Targeted micro-fiber arrays for measuring and manipulating localized multi-scale neural dynamics over large, deep brain volumes during behavior

Highlights

- A new customizable, targeted, and dense micro-fiber array approach for behaving mice

- Measurements and manipulations of distributed neural dynamics over large 3D volumes

- Modality-specific patterns of striatum-wide dopamine release in response to salient stimuli

- Spatial mapping of a behavioral function via serially targeted striatum stimulations

Authors

Mai-Anh T. Vu, Eleanor H. Brown, Michelle J. Wen, ..., Ian G. Davison, David A. Boas, Mark W. Howe

Correspondence

mwhowe@bu.edu

In brief

Vu et al. present a customizable approach using small-diameter optical fibers that enables dense measurements and targeted manipulations of distributed neural activity over large 3D volumes at a spatial resolution and coverage previously inaccessible. They reveal modality-specific spatiotemporal patterns of striatum-wide dopamine release in response to sensory stimuli and precise mapping of a specific behavior onto striatal location.

CellPress

Neuron

NeuroResource

Targeted micro-fiber arrays for measuring and manipulating localized multi-scale neural dynamics over large, deep brain volumes during behavior

Mai-Anh T. Vu,[1,2] Eleanor H. Brown,[3] Michelle J. Wen,[1,4] Christian A. Noggle,[1,2] Zicheng Zhang,[5] Kevin J. Monk,[5] Safa Bouabid,[1,2] Lydia Mroz,[1,6] Benjamin M. Graham,[1] Yizhou Zhuo,[7,8,9] Yulong Li,[2,7,8,9] Timothy M. Otchy,[5] Lin Tian,[2,10] Ian G. Davison,[5] David A. Boas,[11] and Mark W. Howe[1,2,12,*]

[1]Department of Psychological & Brain Sciences, Boston University, Boston, MA, USA
[2]Aligning Science Across Parkinson's (ASAP) Collaborative Research Network, Chevy Chase, MD, USA
[3]Graduate Program for Neuroscience, Boston University, Boston, MA, USA
[4]Howard Hughes Medical Institute, Department of Neurobiology, Harvard Medical School, Boston, MA, USA
[5]Department of Biology, Boston University, Boston, MA, USA
[6]Northeastern University, Boston, MA, USA
[7]State Key Laboratory of Membrane Biology, Peking University School of Life Sciences, Beijing, China
[8]PKU-IDG/McGovern Institute for Brain Research, Beijing, China
[9]Peking-Tsinghua Center for Life Sciences, Beijing, China
[10]Max Planck Florida Institute of Neuroscience, Jupiter, FL, USA
[11]Department of Biomedical Engineering, Boston University, Boston, MA, USA
[12]Lead contact
*Correspondence: mwhowe@bu.edu
https://doi.org/10.1016/j.neuron.2023.12.011

SUMMARY

Neural population dynamics relevant to behavior vary over multiple spatial and temporal scales across three-dimensional volumes. Current optical approaches lack the spatial coverage and resolution necessary to measure and manipulate naturally occurring patterns of large-scale, distributed dynamics within and across deep brain regions such as the striatum. We designed a new micro-fiber array approach capable of chronically measuring and optogenetically manipulating local dynamics across over 100 targeted locations simultaneously in head-fixed and freely moving mice, enabling the investigation of cell-type- and neurotransmitter-specific signals over arbitrary 3D volumes at a spatial resolution and coverage previously inaccessible. We applied this method to resolve rapid dopamine release dynamics across the striatum, revealing distinct, modality-specific spatiotemporal patterns in response to salient sensory stimuli extending over millimeters of tissue. Targeted optogenetics enabled flexible control of neural signaling on multiple spatial scales, better matching endogenous signaling patterns, and the spatial localization of behavioral function across large circuits.

INTRODUCTION

Neural dynamics supporting perception, decision-making, action, and learning vary across multiple spatial scales in the mammalian brain, within and across brain regions. An ongoing technical challenge in systems neuroscience is to measure and manipulate cell-type- and neurotransmitter-specific dynamics at scale in the context of behavior. Toward this goal, wide-field microscopy has enabled millimeter-scale functional imaging with genetically encoded indicators and targeted optogenetic manipulations across nearly the entire superficial cortex of rodents.[1–7] Wide-field microscopy studies have revealed large-scale signaling patterns correlated with simple and complex features of behavior and perception that vary in time over millimeters of brain tissue. Optogenetic manipulations designed to match the scale of these patterns have causally linked large-scale cross- and within-region signaling with behavior.[5] However, optical access to rapid neural dynamics in brain regions deeper than ~1 mm is limited by scattering and requires tissue penetration.[8,9]

GRIN (gradient-index) lenses or optical cannulae are commonly used for cellular-resolution imaging and manipulations from deep brain regions, but these are limited to only small (~0.5–1 mm) fields of view and require significant damage to overlying tissue.[8,10] Alternatively, optical fibers can be used to deliver and collect light from deep brain regions, permitting fluorescent measurements (fiber photometry) and optogenetic manipulations of population signals or neurotransmitter release near the tip of the fiber.[11,12] Although fibers do not provide cellular resolution, their diameters are significantly smaller than

GRIN lenses, presenting a possible utility for accessing larger-scale population dynamics. Moreover, the spatial resolution of fiber photometry is well suited for measuring regional variations in neuromodulator release with fluorescent sensors.

Typical fiber photometry and optogenetic manipulation experiments use only one or two optical fibers targeting a single brain sub-region. Although fiber photometry experiments can provide information about dynamics in a targeted region during behavior, they provide a limited view of how dynamics are coordinated in space across functionally heterogeneous, extended circuits, such as the striatum. Single- or dual-fiber optogenetics experiments, similarly, do not enhance or impair the natural spatial patterns of activity and thus may result in misleading findings, particularly in the case of null results. Without prior knowledge of where task-relevant dynamics are localized, fiber photometry measurements and optogenetic manipulations may be incomplete or mis-targeted. Another complication of interpreting traditional photometry and optogenetics experiments is that standard fibers transmit and collect light from a relatively large volume around the fiber tip,[13] limiting spatial resolution and perhaps obscuring functional heterogeneities within the collection volume.

Recent advances in multi-fiber approaches have attempted to address the problem of spatial scale by increasing the number of implanted fibers to 12–48.[14,15] However, these techniques employ conventional large-diameter fibers (100–200 μm) and thus are not capable of high-density measurements or targeted manipulations across single brain structures without causing significant tissue damage. Additionally, existing implant designs involve rigid, linear arrays with fixed spacing; require specialized connectors; and do not permit flexible targeting of arbitrarily spaced regions.[14] Limitations in the scalability and spatial resolution of existing techniques are particularly problematic for investigating large deep brain structures such as the striatum, which is known to exhibit heterogeneous signaling and control diverse behavioral functions on spatial scales ranging from 100s of microns to millimeters.[16–20] Small-diameter fiber implants offer the possibility of denser recordings but must address targeting and signal detection challenges.[21] Here, we report a scalable new optical fiber array approach using small-diameter fibers capable of measuring and manipulating robust signals from multiple fluorescent sensors at over 100 targeted locations simultaneously over deep three-dimensional volumes in behaving mice.

RESULTS

Micro-fiber array design

To enable precise, high-density targeting of many locations throughout arbitrarily sized deep brain volumes, we designed an implant capable of holding small-diameter (37 or 50 μm O.D.) optical fibers with custom spacing in 3 dimensions (Figure 1A). We successfully tested implants holding 30–103 fibers. The total tissue volume displaced by the fiber arrays is comparable to single or dual implants of conventional large-diameter (200 or 400 μm) optical fibers and less than standard (0.5–1.5 mm) GRIN lenses. For example, a single 400-μm diameter optical fiber displaces a cylindrical tissue volume equivalent to 64

50-μm diameter fibers. We assessed tissue damage around implanted fibers with postmortem immunolabeling and confirmed that there was no significant reduction in neuronal density under 50-μm fiber tips or between neighboring fibers, relative to unimplanted tissue (Figure S1). We primarily designed implants to cover locations across the striatum volume, but arrays can be flexibly fabricated to cover any combination of desired brain regions with custom density and fiber counts. The smaller-diameter fibers sample fluorescence from significantly smaller tissue volumes than conventional fibers, allowing for denser optical measurements at higher resolution[13] (Figure S2A). Fibers were separated by a minimum of 250 μm axially and 220 μm radially, ensuring no significant overlap between fiber collection fields, as confirmed by previous empirical and analytical measurements.[13,22,23] Fibers were then arranged through holes in a micro-3D-printed, biocompatible plastic grid, and proximal ends were glued within a polyimide tube and then cut and polished to form a smooth bundle surface for imaging (Figures 1A and 1B). To enable optical measurements of cell-type- and neurotransmitter-specific signaling, mice were injected at multiple locations with AAVs to drive the expression of genetically encoded fluorescent indicators (e.g., dLight1.3b,[24] GCaMP7f,[25] and Ach3.0,[26] Table S1).

Chronic measurements of large-scale calcium and neuromodulator signals in head-fixed mice

Mice were outfitted with metal head plates during array implantation to allow for fiber imaging via a table-mounted microscope during head-fixed behaviors on a floating 2D treadmill[27] (Figure 1B). Illumination was provided by three high-power LEDs, which could be alternated and synchronized with two CMOS cameras to enable the quasi-simultaneous recording of red and green fluorophores (570 and 470 nm, respectively, Figure S2C) and an isosbestic control (405 or 415 nm) for motion and hemodynamic artifacts. We initially validated the ability of our fiber arrays to reliably detect changes in cell-type-specific Ca^{2+} signaling across the striatum using the genetically encoded sensor GCaMP7f expressed selectively in D1 spiny projection neurons (Figure 1C). Spontaneous Ca^{2+} transients during locomotion were observed across locations that were clearly separable from noise and highly heterogeneous across locations (Figure 1C). These transients reflected spatially weighted Ca^{2+} signals from neuron populations within a small volume around the fiber tips (Figure S2A).[13,28–30] Pairwise correlations of SPN Ca^{2+} signals were generally low but were highly variable and dropped off significantly with distance between fibers (Figure S2D). No relationship was observed between signal correlations and distance on the bundle surface after accounting for brain distance, indicating no cross talk between nearby fibers in the bundle (Figures S2E and S2F). Auto-fluorescence was very low and consistent across our fibers compared with the baseline sensor fluorescence (Figures S5G and S5H). Transients were not observed with illumination at the 405-nm isosbestic point, indicating minimal contribution from hemodynamic or motion artifacts (Figure 1C). Robust, striatum-wide signals were also obtained with optical sensors for dopamine (DA) and acetylcholine (Figure S2C) and for 37-and 50-μm-diameter fibers (Figure S2B). DA release at a single location in response to
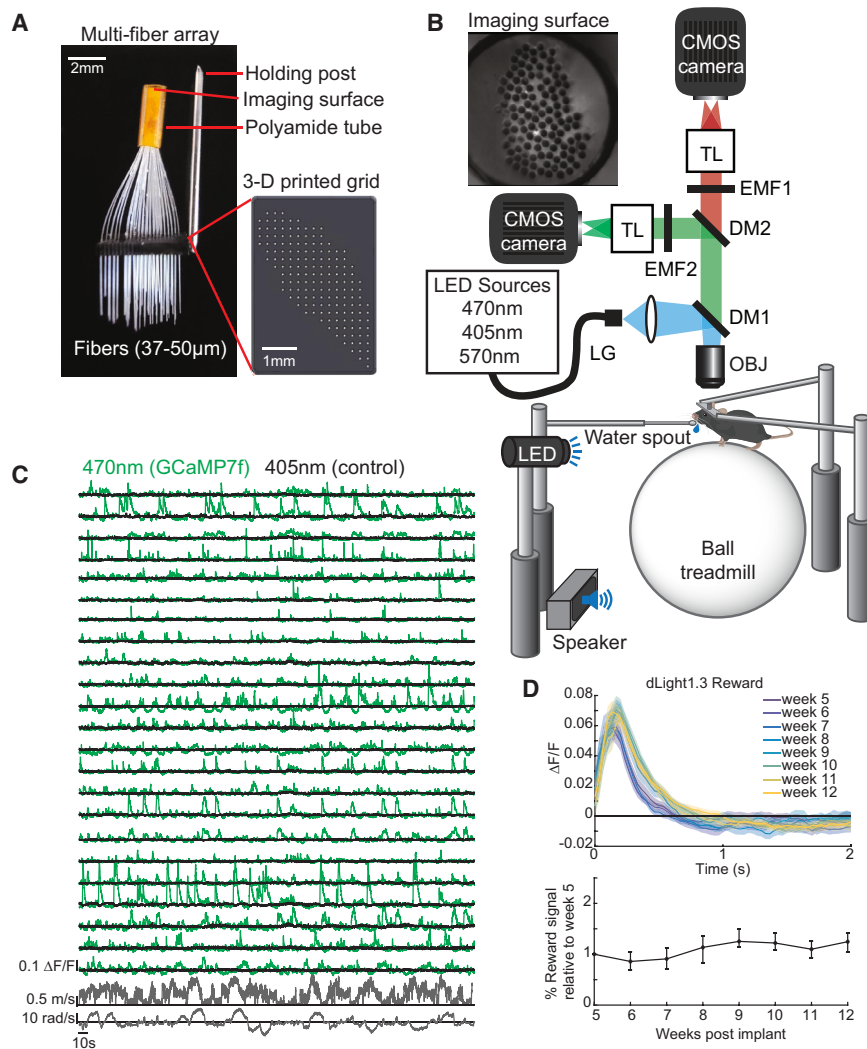
Figure 1. Multi-fiber arrays for large-scale optical measurements across deep brain volumes in behaving mice

(A) Multi-fiber array design.

(B) Schematic of the microscope design for fiber bundle imaging (inset) in head-fixed behaving mice. TLs, tube lens; EMF, emission filter; DM, dichroic mirror; OBJ, objective. See STAR Methods for details on each component.

(C) Changes in GCaMP7f fluorescence (ΔF/F) measured from 23 example fibers in a 93-fiber array implanted in the striatum of a D1-cre mouse. 470 nm excitation light (green trace) was alternated with 405 nm light (black) at 18 Hz to provide a quasi-simultaneous isosbestic control. Significant transients are absent with 405 illumination. Bottom: angular and linear treadmill velocity.

(D) Top: mean changes in peak dLight1.3b fluorescence (DA release) from a single representative fiber aligned to unpredicted water reward consumption at different time points up to 12 weeks post-array implantation. Shaded regions, SEM. Bottom: median peak reward ΔF/F across fibers (n = 44 fibers) in one mouse, normalized to initial responses on week 5. Upper and lower error bars are the 75th and 25th percentiles, respectively.

See also Figures S1 and S2.

(Figures S1 and S7C; see STAR Methods). CT images were scaled and aligned to a common coordinate framework[32] to combine measures across mice (Figures 2B–2E; see STAR Methods). We quantified the displacement for each localized fiber tip relative to its intended target in the brain and found that the magnitudes and types of targeting errors varied across mice and fibers (Figure S3). Targeting errors could result from the translation of the grid position relative to target structures and from the non-uniform trajectories of individual fibers through the brain during implantation (Figure S3). Although our micro-CT-based localization strategy allows for efficient and precise reconstructions of the high-density arrays, conventional histological localization may be a viable alternative for sparser array designs if micro-CT capabilities are not available (see STAR Methods and discussion).

unpredicted water reward delivery was highly reliable and comparable in amplitude over at least 12 weeks following stable expression of dLight1.3b, confirming the utility of this approach for chronic measurements (Figure 1D).

## Micro-CT-based method for precise fiber localization and atlas alignment

As the fibers were densely spaced and smaller and more flexible than larger fibers, conventional histological techniques for fiber localization were not feasible. Therefore, we utilized a multi-step approach to first map each fiber on the array to the imaging surface pre-implantation (Figure 2A) and then localize the tips of each fiber in the brain postmortem (Figures 2B–2E). For postmortem localization, we used micro-computed tomography (CT) scanning, which allowed partially automated tracing of each fiber to the grid surface and precise identification of the fiber tip with approximately 10-μm resolution (Figures 2B and 2C). Tissue visualization via CT was enabled by soaking the brains in a Lugol's solution prior to scanning to enhance contrast.[31] This contrast agent is compatible with immunohistological staining

Chronic measurements of large-scale calcium and neuromodulator signals in freely moving mice

To enable fiber array measurements in freely moving animals, we attached "miniscopes"[34,35] above the fiber bundle implant and monitored fluorescence across fibers as animals explored a behavioral arena (Figure 3A). This revealed robust, high-SNR signals from GCaMP7f expressed in D1 spiny projection neurons that varied dynamically during locomotion (Figure 3B). Activity was highly heterogeneous, indicating complex activity dynamics across the volume of the striatum. We also
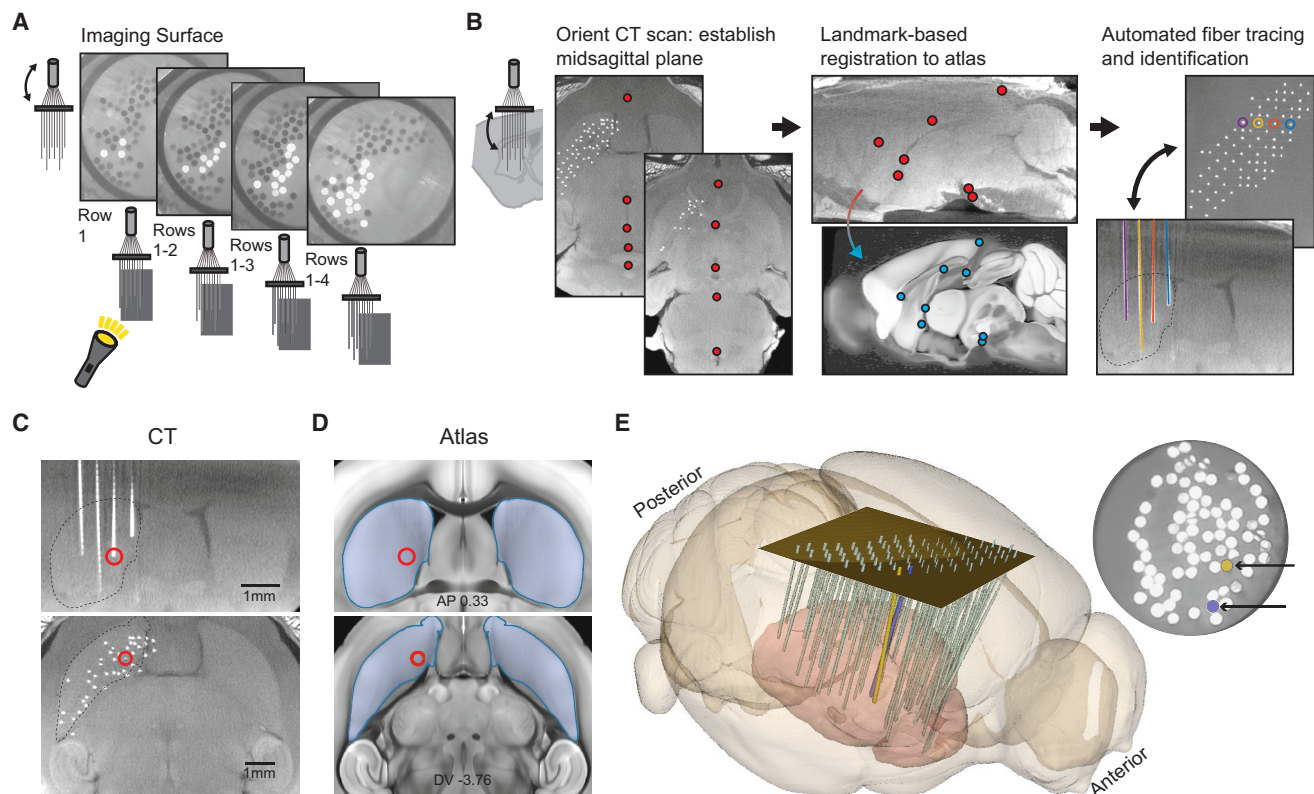
Figure 2. Calibration and postmortem localization of micro-fiber arrays over deep brain volumes with computerized tomography

(A) Pre-implant calibration procedure for matching each fiber grid position with the corresponding location on the imaging surface. Example photos show the imaging surface as light is shone through subsequently uncovered rows at the distal implanted ends. This process was then repeated for columns. Images of illuminated fibers were used to match the fibers' position on the grid surface (i.e., row and column location) with the imaging surface.

(B) Schematic of the postmortem localization procedure. Left: micro-CT scans in the horizontal plane in two different example axial locations with manually placed markers (red dots) to identify the position of the midsagittal plane for proper orientation. Middle: micro-CT scan in the sagittal plane with some example manually placed markers for identified anatomical markers to enable registration to the Allen Mouse Brain Common Coordinate Framework atlas[32] (bottom). Right: micro-CT scans in the horizontal plane of the grid surface (top) and coronal plane (bottom) showing the resulting automated tracing of 4 optical fibers.

(C) Fiber tip localization. Micro-CT scan images in the coronal (top) and horizontal (bottom) planes from a mouse implanted with an 83-fiber array of 50 μm fibers targeting the striatum. Red circles indicate the location of one fiber tip in both planes.

(D) Coronal (top) and horizontal (bottom) plane atlas images corresponding to the locations of the registered CT images in (C). Circles indicate the localized position of the highlighted fiber in (C).

(E) 3D reconstruction (created with 3DSlicer[33]) showing atlas-aligned reconstructions based on the CT images of every fiber in a 74-fiber array. Colored fibers (blue and yellow) crossed in the brain but were still unambiguously traceable back to the grid surface and thus also the imaging surface.

See also Figure S3.

used miniscope imaging to monitor striatal DA release with dLight1.3b as mice foraged for food rewards. Interestingly, this revealed large transients that appeared to be reliably associated with the initial approach toward food rewards prior to consumption (Figure 3C).

Spatial topography of modality-specific DA release magnitudes over large-scale three-dimensional volumes

To demonstrate the utility of our fiber array method in resolving large-scale spatial and temporal patterns of neural signaling, we measured striatum-wide DA release in response to salient stimuli using the fluorescent DA sensor dLight1.3b[24] (Figure 4A). Midbrain DA neurons exhibit short latency responses to salient visual and auditory stimuli, which may drive learning, spatial attention, or orienting responses.[36–38] Fiber photometry studies have established that salient, high-intensity stimuli evoke short latency increases in the posterior striatum and decreases in the anterior ventral striatum in mice.[39] However, standard approaches have not permitted the investigation of sensory-evoked DA release at striatum-wide scales. Mice were presented with either visual (blue LED) or auditory (12 kHz tone) stimuli at random intervals (4–40 s) (Figure 4C). Surprisingly, the tone and light stimuli evoked distinct, modality-specific, spatiotemporal patterns of DA release across striatum locations (Figures 4B–4H). The light evoked transient increases in DA release across many locations with an amplitude gradient extending from the anterior striatum into the posterior tail, where increases were less prevalent and of smaller amplitude (Figures 4B, 4D, 4E, and S4A). In contrast, the tone evoked the
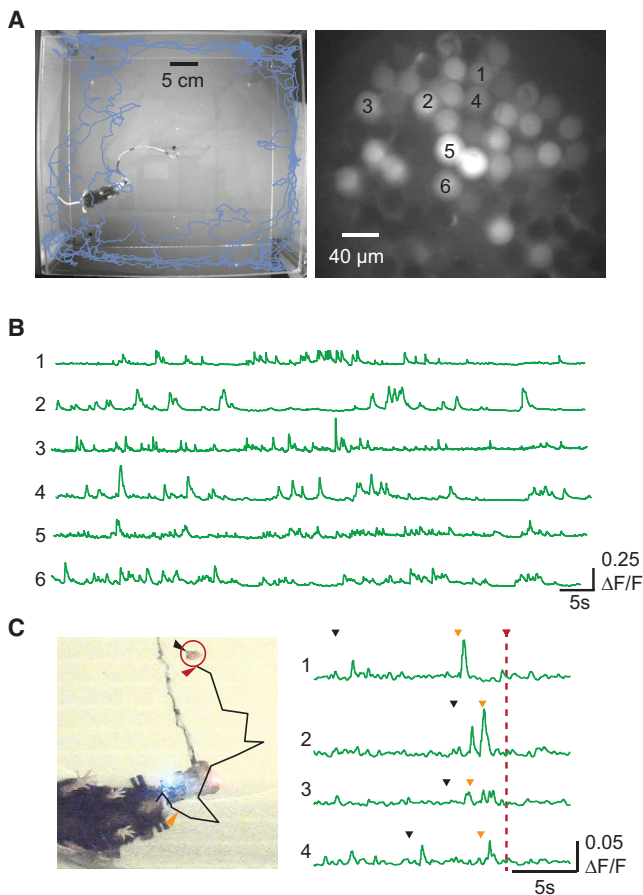
Figure 3. Miniscope imaging of multi-fiber arrays in freely moving mice

(A) Locomotor trajectory of a miniscope-implanted mouse (left) and view of the fibers imaged with the miniscope (right).

(B) Example GCaMP7f fluorescence traces (ΔF/F) from 6 fibers with robust signal in a D1-cre mouse.

(C) Path of a mouse (left) converging on a food reward (red circle) during dLight1.3b (DA) imaging (right), along with example ΔF/F traces from one fiber over 4 food deliveries aligned to the onset of consumption (red arrows). Black arrows indicate when the food was dropped into the arena; orange arrows indicate the estimated beginning of approach.

strongest increases in DA release at sites in the posterior tail, whereas anterior to the tail, the tone evoked primarily decreases in DA release (Figures 4B, 4D, 4F, and S4C) Decreases were slightly more prevalent in the anterior lateral and ventral striatum, with many sites exhibiting both increases to the light and decreases to the tone (Figures 4E and 4F). These distinct release patterns were consistent within and across mice (Figures S4A and S4C). Locomotor changes in response to stimuli were variable, bi-directional, and differed across mice and individual stimulus presentations, whereas DA release patterns in response to light and tone were consistent, indicating that modality-specific patterns were stimulus, and not movement, driven (Figure S4). Large fluorescence changes and spatial patterns were not observed with 405- or 415-mn (approximate dLight1.3 isosbestic point) illumination, ruling out a significant impact of hemody-

namic changes on the spatial DA release patterns (Figure S5). These data indicate that representations of stimulus saliency in striatal DA release are spatially organized by stimulus modality and polarity across striatum regions.

Modality-specific gradients of DA release timing across the striatum

The simultaneous parallel recordings and high spatial resolution afforded by our multi-fiber arrays enable the investigation of how distributed neural signals are coordinated in time across neural space. A previous study has reported wave-like dynamics of reward-related striatal DA release in 2-dimensions in the dorsal striatum.[40] We assessed whether spatially organized temporal gradients were present for salient stimulus-evoked DA release across the three-dimensional striatum volume. Response latencies (from stimulus onset to the half-max or half-min amplitude) were shorter, on average, for DA increases in response to light and shorter for DA increases than for decreases in response to the tone but varied considerably (Figures 5A and 5B, light increase mean latency 221.6 ms, SD 42.5; tone increase mean latency 305.4 ms, SD 100.0; tone mean decrease latency 428.3 ms, SD 197.1). We examined whether temporal structure was present across simultaneously recorded locations by comparing the trial-to-trial latencies of the DA responses to salient stimulus presentations. DA release latencies (time to half-max) for light presentations followed a spatial gradient along the anterior-posterior axis, with relatively faster latencies to increase in the anterior striatum than in the posterior striatum, consistent with wave-like dynamics (Figures 5C, 5E, and 5G). DA release latencies to tone presentations followed a different spatial gradient with faster latencies in the posterior striatum relative to the anterior striatum (Figures 5D, 5F, and 5H). The posterior-anterior spatial gradient in the tone release latencies could be attributed to the decreases in the anterior striatum occurring at a longer latency than increases in the posterior tail (Figures 5B, S6A, and S6B). Subtle spatial structure along the M/L and D/V axes was observed for tone DA increase and decrease latencies in the anterior striatum and tail, respectively, when considered independently (Figures S6A and S6B). Spatial gradients were also present at the level of individual mice (Figures S6C and S6D). These data suggest that striatal DA release in response to salient stimuli propagates through the striatum with wave-like dynamics in modality-specific spatial gradients.

Targeted light delivery to individual microfibers for localized optogenetic manipulations

The DA release measurements above illustrate that bi-directional neuromodulatory signals that may modulate movement, perception, and learning are heterogeneously expressed across arbitrarily shaped three-dimensional volumes in the striatum (Figures 4 and 5). Precisely assessing the impact of large-scale neuromodulator release on behavior requires targeted manipulations that match the spatial and temporal properties of the endogenous release, which is not possible with standard optogenetic manipulations with large-diameter optical fibers. To enable flexible and targeted optogenetic manipulations of 3D
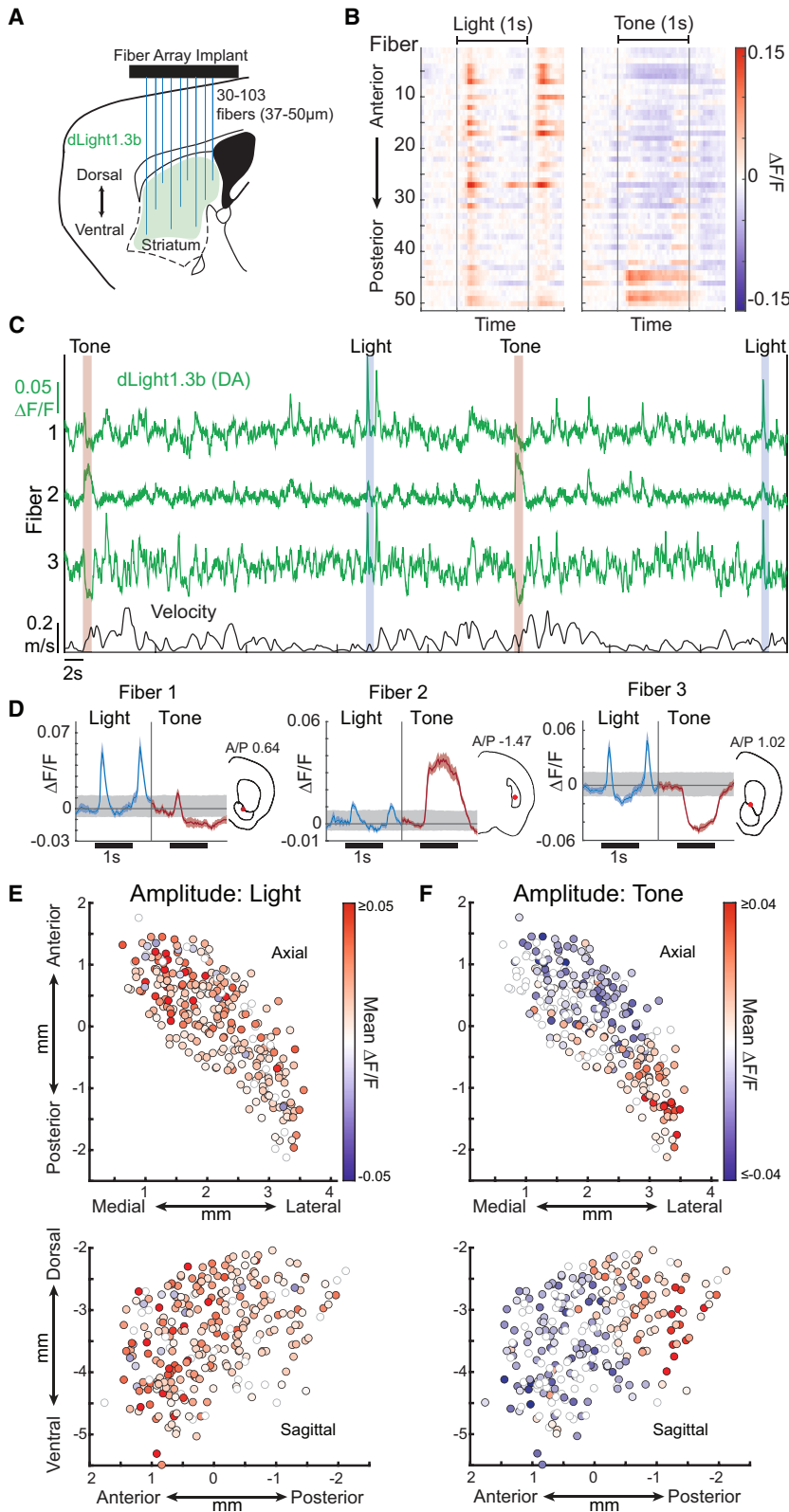
Figure 4. Modality-specific patterns of the amplitude of striatum-wide dopamine release in response to salient stimuli

(A) Implant schematic for striatum-wide measurements of DA release with dLight1.3b.

(B) ΔF/F (dLight1.3b) across all fibers (rows organized anterior to posterior from top to bottom) for single representative light (left) and tone (right) presentations.

(C) ΔF/F traces from 3 example fibers from a single mouse (out of 280 fibers from 7 mice) during multiple presentations of light and tone stimuli.

(D) Triggered averages of ΔF/F across all stimulus presentations (n = 18 each for light and tone) for the 3 fibers shown in (C). Insets show brain locations of each fiber. Shaded regions, SEM. Gray-shaded band, 0.5–99.5th percentile of bootstrapped null distribution.

(E) Largest amplitude mean ΔF/F change across all light presentations for all fibers (n = 280) and mice (n = 7, 4F + 3M) in a 1-s window after stimulus onset. The color of each circle represents the largest mean ΔF/F change for a single fiber in either the positive or negative direction. The location of each circle indicates its localized fiber position in the axial (top) and sagittal (bottom) planes. Open circles, non-significant increases or decreases relative to baseline (significance: mean exceeding 99% confidence interval of the bootstrapped null distribution for 3 consecutive time points, $p < 1.0 \times 10^{-6}$).

(F) Same as (E), for tone presentations.

See also Figures S4 and S5.
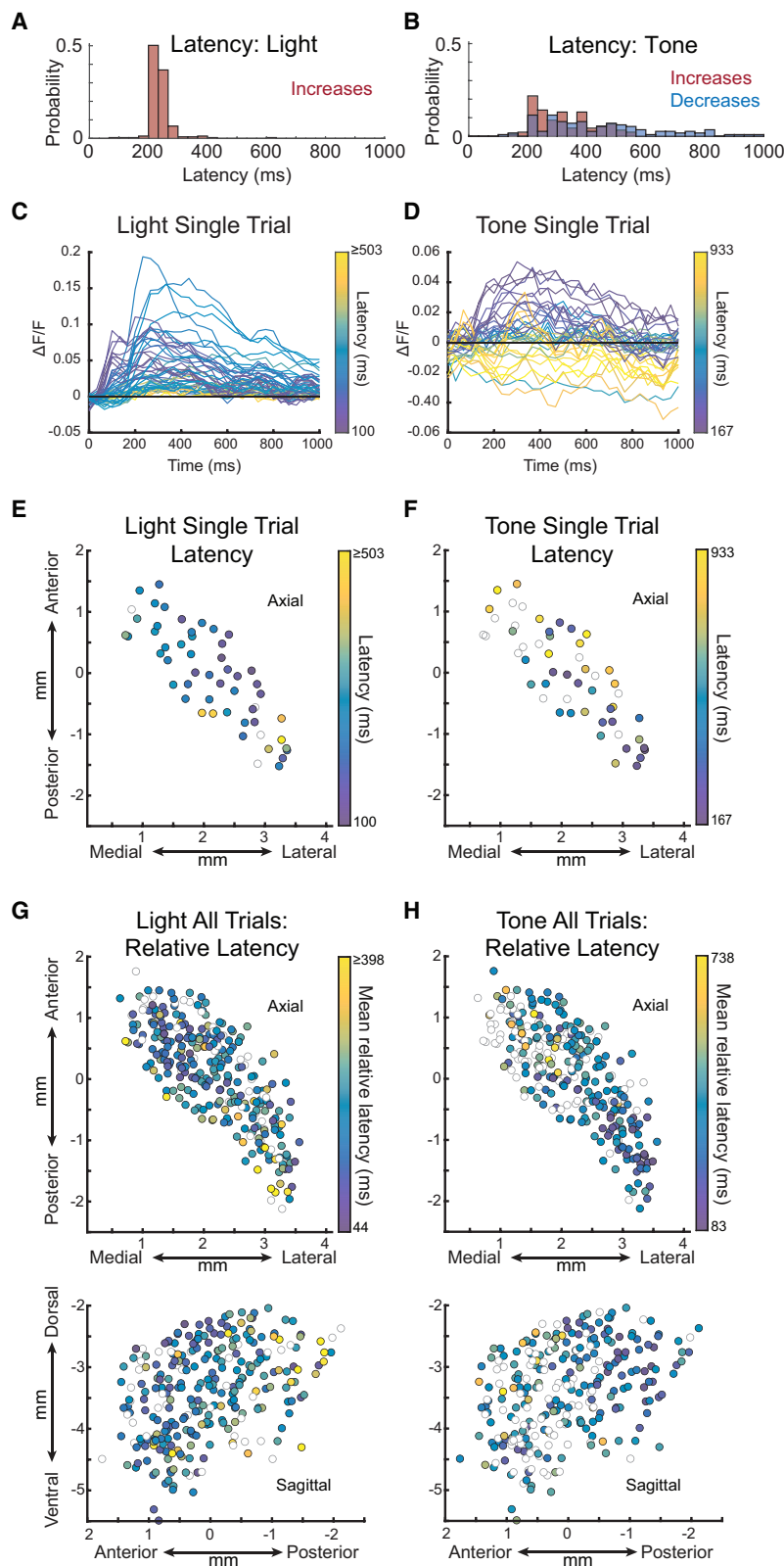
Figure 5. Temporal organization of modality-specific striatum-wide dopamine release in response to salient stimuli

(A) Histogram of latencies to the half-max amplitude of the triggered average response to the light.

(B) Histogram of latencies to the half-max amplitude of increases (red) or half-min amplitude of decreases (blue) of the triggered average response to the tone.

(C) ΔF/F for a single light presentation across all fibers (n = 49/53) showing a significant response (single trial activity and mean triggered average exceeding 99% confidence interval of the bootstrapped null distribution for 3 consecutive time points, p < 1.0 × 10⁻⁶). Traces for each fiber are colored according to the latency from stimulus onset to the half-max amplitude.

(D) Same as (C), but for a single tone presentation (n = 38/53 fibers). Latency was calculated from the stimulus onset to the half-max or half-min amplitude for fibers that increased or decreased, respectively.

(E) Spatial map in the axial plane of the half-max latencies from (C).

(F) Spatial map (as in E) of the half-max or half-min latencies from (D).

(G) Spatial map of the mean relative half-max latencies of DA release for each fiber normalized to the minimum, half-max latency for each trial across all light presentations for all fibers (n = 280) and mice (n = 7, 4F + 3M, same mice as Figure 4). The color of each circle represents the mean relative latency for a single fiber. Open circles in spatial maps are non-significant increases or decreases relative to baseline (significance: mean triggered average exceeding 99% confidence interval of the bootstrapped null distribution for 3 consecutive time points, p < 1.0 × 10^×6).

(H) Same as (G), but for tone presentations. For fibers with significant decreases, the half-max latency to the minimum is shown (see Figures S6A and S6B).

See also Figure S6.
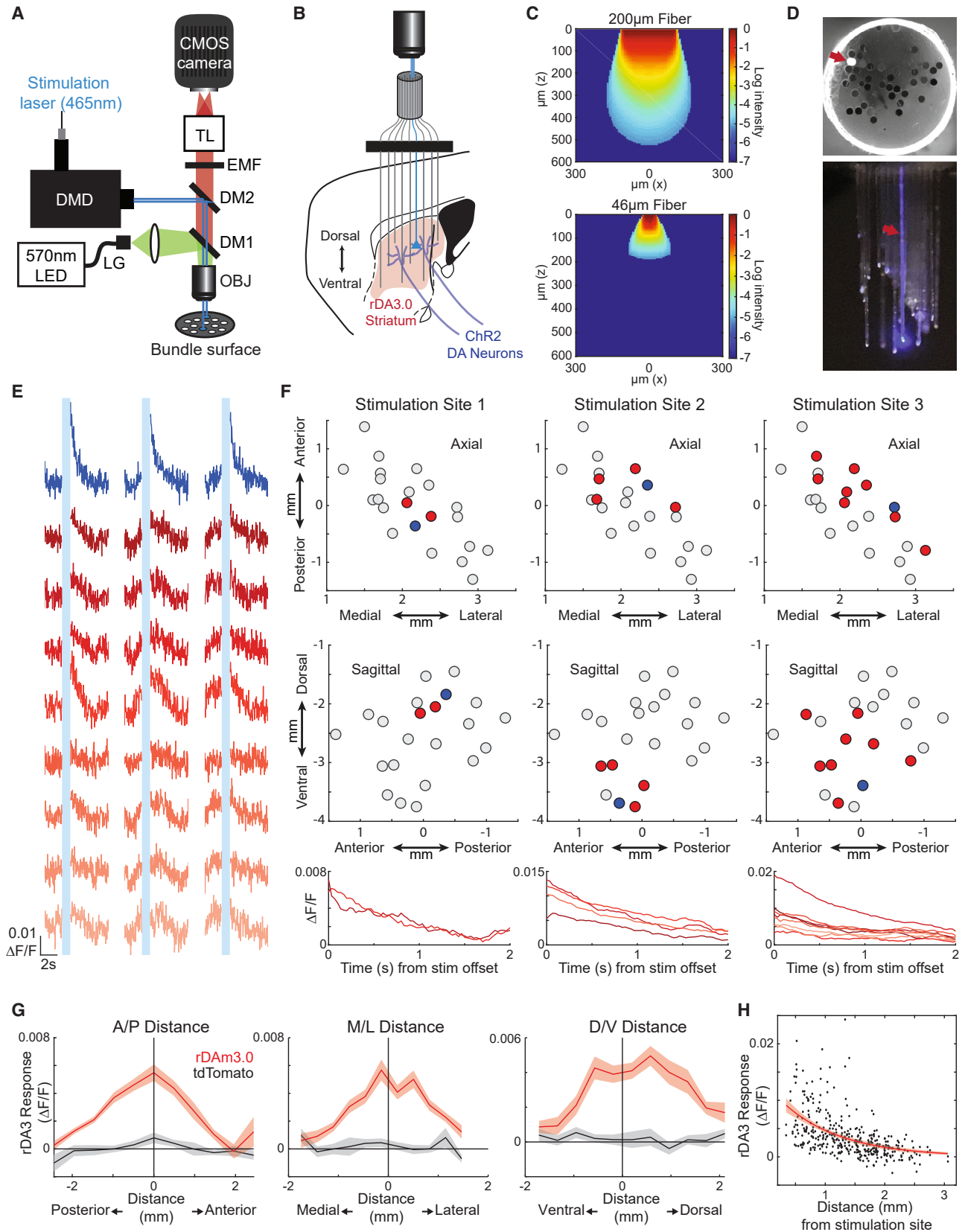
volumes, we incorporated a programmable digital mirror device (DMD, Mightex Polygon) into our microscope to target laser light (465 nm) into individual optical fibers (Figures 6A, 6B, and 6D). We tested the ability of this system to control local striatum DA release by expressing the excitatory opsin channelrhodopsin-2 (ChR2) in midbrain DA neurons and the red DA sensor rDAm3.0[41] across the striatum (Figure 6B). A fiber array was then implanted to target locations across the striatum volume. We confirmed that circular light spots could be targeted to individual optical fibers with no leak into neighboring fibers (Figure 6D). Light spot power at the objective ($\sim$750 μW) was calibrated to achieve a power density at the fiber tip of $\sim$175 mW/mm^2, which is estimated to activate ChR2-expressing axons in a volume extending approximately 150 μm axially from the bottom of the fiber tip (Figure 6C). This activation volume is significantly ($>10\times$) smaller than the volume activated by the same power density through a standard 200-μm, 0.37-NA fiber (Figure 6C). A 570-nm LED was continuously projected onto the fiber bundle surface to excite rDAm3.0. The low power (1.6–2 mW/mm^2 at the tip) of the 570-nm excitation light and very low photoactivation of ChR2 at this wavelength ensured no stimulation during imaging.

Local control of striatal DA release through micro-fiber arrays

To measure the spread of evoked DA release in response to terminal stimulation through individual fibers, we delivered light bursts (1 s duration, 30 Hz, 4 ms pulse width) to individual fibers while measuring DA release across neighboring locations. Large increases in fluorescence were observed at the site of stimulation, but these signals were partly contaminated by the known photoswitching properties of the rDAm3.0 sensor,[43] as we observed significant increases in non-opsin-expressing mice (Figures 6E and S7A). Photoswitching in controls, but not opsin-expressing mice, was entirely confined to the stimulated site (0/22 non-stimulated sites for 3 single-site stimulations,

bootstrap test vs. null distribution, see STAR Methods), so we focused our analysis on the spread of stimulated release to non-stimulated fibers. Significant transient increases in stimulation-evoked DA release were detected at sites neighboring the targeted fiber, which dropped off sharply with distance in all 3 dimensions (Figures 6E–6H). These results were not affected by DA-dependent changes in hemodynamics, as there were no significant stimulation-evoked fluorescent increases in control mice, which were injected with tdTomato instead of rDAm3.0 (0/48 non-stimulated sites for 26 single-site stimulations across 2 mice, bootstrap test vs. null distribution). Given the localized activation volume through our fibers (Figure 6C) relative to our fiber spacing (>350-μm separation), this DA release spread was not likely due to direct light propagation to neighboring fibers but to the highly branched morphology of DA axons.[44] Supporting this idea, activation dorsal to the stimulation location dropped off less with distance than activation ventral to the stimulation location (Figure 6G, D/V distance, right), which would not be expected based on the excitation profile (Figure 6C) but is consistent with the dorsally extending axon morphology of branching DA axons.[44] Thus, our fiber array method provides semi-localized control of neuromodulator release in the striatum, enabling combinatorial stimulation to mimic the spatial and temporal spread of natural release in response to events such as salient stimulus presentation (Figure 4).

Targeted optogenetic manipulations can localize region-specific behavioral effects in the striatum at multiple scales

Many large brain regions, such as the striatum and hippocampus, are composed of functionally distinct circuits and cell types, which provide parallel control over distinct aspects of behavior. In the striatum, for example, regionally restricted activation of D1-expressing spiny projection neurons (dSPNs) can drive the execution of specific actions.[18] Closely spaced circuits (<1 mm separation), either within or across regions, cannot be

---

Figure 6. Light targeting to individual fibers permits localized optogenetic manipulations of striatal dopamine release

(A) Schematic of the microscope design and light path for simultaneous single-site stimulation and imaging. TL, tube lens. EMF, emission filter, DM, dichroic mirror, OBJ, objective, LG, liquid light guide, DMD, digital mirror device (see STAR Methods for details).

(B) Schematic of injection and implant strategy. rDAm3.0 was expressed throughout the striatum, whereas ChR2 was expressed in DA neuron axons. Fiber array implant targeted multiple sites throughout the striatum. Laser light was targeted to a single fiber to stimulate local DA axons.

(C) Relative excitation light (465 nm) intensity modeled as a function of distance from the optical fiber tip for a standard 200-μm diameter, 0.37-NA fiber (top) and the 50-μm diameter fibers used in our arrays[42] (bottom). Intensity values are shown only for locations estimated to achieve a power density sufficient to activate ChR2 (1 mW/mm^2).

(D) Top: LED-illuminated fiber bundle surface with blue laser light targeted to a single fiber (red arrow). Bottom: distal, implanted ends of a fiber array. A single fiber is illuminated (red arrow), illustrating restricted targeting.

(E) ΔF/F traces across fibers for three example stimulation trials at a single site (blue trace, top) and all other recording sites with a significant response to stimulation (bootstrap test, $p < 1.0 \times 10^{-6}$), ordered from top to bottom by their total distance from the stimulation site (shaded from dark to light red). Vertical light blue bars indicate laser periods (4 ms pulses at 30 Hz for 1 s).

(F) Spatial maps (axial, top; sagittal, middle) of significant changes in DA release (ΔF/F) for three example stimulation sites (stimulation site 3 is the same as E). Each circle is a single recording site, with the stimulation site in blue, sites with a significant evoked response (bootstrap test, $p < 1.0 \times 10^{-6}$) in red, and sites lacking a significant response in gray. Bottom: mean ΔF/F triggered on stimulation offset at all of the sites with a significant response (left, n = 7 trials; middle, n = 9 trials; right, n = 9 trials). Color is ordered by distance from the stimulated fiber (darker colors indicate closer to the fiber).

(G) Mean ΔF/F to single-site stimulation binned by distance from the illuminated fiber across 3 anatomical axes in experimental mice expressing DAm3.0 (red) and control mice expressing tdTomato (black). Shaded region, SEM (n = 378 for 1 DAm3.0 mouse; 21 recording sites per stimulation, 18 stimulation sites. n = 338 for 2 tdTomato mice; 27 and 19 recording sites per stimulation, 9 and 5 stimulation sites, respectively).

(H) Mean ΔF/F for each non-stimulated fiber vs. distance from the stimulated fiber for all stimulations. The red line shows the exponential model fit. Shaded region, 95% prediction confidence interval.

See also Figure S7.
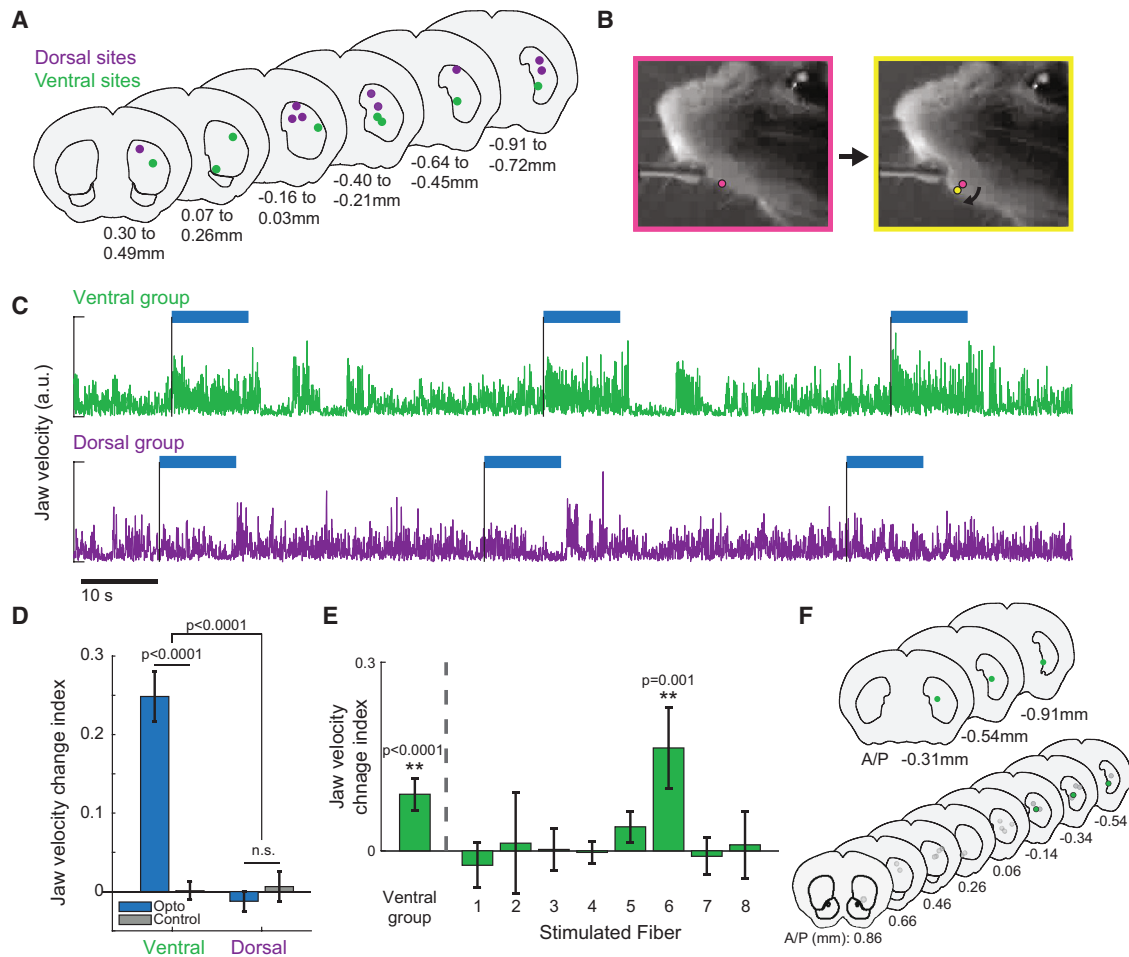
Figure 7. Localized effects of D1 spiny projection neuron stimulation on jaw movements

(A) Coronal cross-sections showing groups of stimulation sites targeted to the dorsal striatum (purple, n = 9) and ventral striatum (green, n = 8) in a mouse expressing ChR2 in D1 SPNs.

(B) Two example live video frames separated by ~66.66 ms, showing a change in jaw position during stimulation at all ventral sites in (A). Pink and yellow markers indicate the front lower jaw marker, labeled automatically using DeepLabCut.

(C) Jaw velocity in pixels/second during stimulation (blue bar, 4 ms pulses at 30 Hz for 10 s) delivered to a group of ventral sites (green, top) or dorsal sites (purple, bottom).

(D) Average jaw velocity change index (see STAR Methods) during stimulation at a group of ventral (left) and dorsal (right) sites in ChR2-expressing mice (blue) and a control mouse (gray). Error bars, SEM (from left to right: n = 84 trials; n = 39 trials; n = 85 trials; n = 42 trials across 3 ChR2-expressing mice and 1 control mouse). Interaction p < 0.0001, 2-way ANOVA; opto vs. control p values, 2-sample t test.

(E) Average jaw velocity change index (as in D) for the stimulation of all the ventral-targeted sites simultaneously (far left) and each ventral site individually for one example mouse (n = 9 trials per stimulation site). Only one site had a significant change index when stimulated individually. **p < 0.01, bootstrap test vs. null distribution. Error bars, SEM.

(F) Top: location in the striatum of sites which had a significant jaw velocity change index when stimulated individually (n = 3 mice, only one fiber from each mouse was significant; also see Figure S7B) Bottom: location in the striatum of all the VLS-targeted stimulation sites, with the 3 fibers from the top shown in green. Each coronal slice here is 200-μm thick and centered on the A/P coordinate indicated.

See also Figure S7.

independently manipulated by existing multi-fiber optogenetic approaches because of the broad light spread and the tissue damage caused by large-diameter optical fibers (Figure 6C). To test whether we could apply targeted optogenetic stimulations to localize regions that control a distinct behavior, we stimulated ChR2-expressing dSPNs at individual locations targeted by our microfibers (Figure 7A). We focused on orofacial movements, as it is known that cortical orofacial projections terminate in distinct ventral striatal regions and that broad stimulation of D1-expressing neurons in those regions can modulate orofacial behavior.[18,45,46] Changes in orofacial movements were quantified by tracking the nose and points along the jaw in live video recordings using DeepLabCut[47,48] (Figures 7B and 7C). To first confirm that we could drive region-specific orofacial changes with broad unilateral stimulation, we coupled light into two groups of fibers targeting the ventral or dorsal striatum (Figure

7A). We found that stimulating regions in the ventral, but not the dorsal, striatum led to rapid increases in jaw movement, which were not present in the non-opsin-expressing control mouse (two-way ANOVA interaction between region and optogenetic stimulation group p = 7.4×10^{-7}, two-sample t test between optogenetic stimulation and control groups: p < 0.01; p = 0.0002, ventral; p = 0.45, dorsal, Figure 7D). These results confirm our ability to broadly localize effects of stimulation to specific striatum regions and are in agreement with the topography of orofacial inputs to the striatum and previous behavioral effects with larger-diameter fibers.[18,45]

We then tested whether we could more precisely localize stimulation to regions driving jaw movements by coupling light into only single-ventral-striatum-targeted fibers at a time. We found that only one of the eight ventral fibers from each mouse produced a significant effect on jaw movements (p < 0.01, n = 3 mice, Figures 7E and S7B). Post hoc CT scanning (Figure 7F) localized these fibers to the posterior medial striatum, a region receiving heavy orofacial projections from the upper mouth regions controlling jaw movement.[45] Most ventral striatum fibers that did not elicit jaw movements were located more anteriorly and medially, in regions that do not receive strong orofacial inputs (Figures 7A and 7F). Interestingly, some fibers in the ventral posterior striatum did not elicit jaw movements, which could reflect micro-heterogeneity across sites. ChR2 expression was confirmed around all stimulated fibers with postmortem histology (Figure S7C). Future experiments can apply this approach to further probe the roles of striatal sub-circuits in controlling distinct actions. These results demonstrate the capability to conduct large-scale surveys of behavioral function across targeted locations within deep tissue volumes extending within and across closely spaced circuits.

DISCUSSION

We developed and applied a new micro-fiber array and localization strategy that enables targeted measurements and manipulations of cell-type- and neurotransmitter-specific signaling across large, deep brain volumes during behavior and learning. This approach provides denser sampling, larger tissue coverage (more fibers), and higher spatial resolution than current multi-fiber methods, enabling the investigation of dynamics and their impact on behavior on new spatial scales. The simple implant design can be easily modified to accommodate more (or less) fibers with any spacing by changing the configuration of the grid patterning (Figure 1A), without modifications to the microscope setup or need for specialized connectors. Flexible scaling of fiber counts and spacing allows for the investigation of within- and cross-region network dynamics over many brain regions in parallel and perhaps across brains of larger species, such as rats or non-human primates. We developed a micro-CT-based localization approach (see resource availability for pipeline and code) to unambiguously localize each fiber in the brain relative to anatomical landmarks and correct for various sources of mis-targeting (Figures 2 and S3). It is possible for those without access to a micro-CT scanner to identify fiber tracks using more conventional histological methods (Figure S1), although accurate localization may require arrays with fewer fibers and/or larger spacing, which can be easily tailored for the desired application (see STAR Methods for more information and recommendations). For example, lower-density arrays may be adequate for experiments investigating large-scale dynamics across multiple brain regions.

Simultaneous, within-animal measurements of widespread network dynamics can reveal the spatial scales over which behaviorally relevant dynamics are expressed. We applied the arrays to map the spread of distinct DA signals to salient auditory and visual cues across the striatum and describe a topography extending across millimeters in 3 dimensions (Figures 4 and 5). Previous studies using single- and dual-fiber photometry have shown similar differences in DA release polarity between the anterior ventral and posterior striatum in response to salient tones but could not resolve how these signals extend across other striatal regions.[39] We also describe a new modality-specific organization in the relative amplitudes and timing of stimulus-evoked DA release (Figures 4 and 5). Simultaneous transmission of distinct, modality-specific positive and negative DA releases to downstream regions may differentially influence learning or immediate action to promote the approach or avoidance of particular cues.[49,50] Understanding how neuromodulatory signals are balanced across regions, on immediate or long-term timescales, will likely be key to predicting their relative influence on downstream structures and ultimately their impact on behavior.

The smaller excitation and collection volume around each fiber tip[13,42] (Figures 6C and S2A) permits a more localized interrogation of closely spaced circuits within or across deep structures. One potential trade-off of this approach is that signals may be more difficult to resolve in sparsely expressing brain regions or cell populations. Localized spatial resolution and wide coverage are particularly important for large, heterogeneous structures, such as the striatum or the hippocampus, where circuit dynamics and behavioral function can vary over unknown scales ranging from hundreds of microns to millimeters.[17,18,20,51–53] The restricted collection volume and dense fiber spacing can also resolve spatiotemporal structure, such as "traveling waves" or spatial synchrony across large volumes, which is not accessible by non-simultaneous, cross-group comparisons. Traveling waves across scales have been observed in multiple cell types and systems and are hypothesized to play important roles in healthy and pathological circuit functions.[11,54–56] Indeed, waves of DA signaling have been described in two dimensions across regions of the dorsal striatum.[40] Our micro-fiber arrays provide an opportunity to resolve the propagation of waves accessible by fluorescent sensors and time varying synchrony across large volumes in 3 dimensions. Simultaneous multi-site measurements were applied to resolve 10s of ms-time-scale temporal offsets in modality-specific stimulus-evoked DA release across the striatum volume (Figures 4 and 5). These results indicate wave-like patterns of bi-directional DA release, which may reflect distinct signals that may differentially regulate learned and intrinsic responses to salient stimuli in downstream regions.

Drawing links between naturally occurring dynamics and behavior requires targeted circuit manipulations that accurately match the spatiotemporal characteristics of the dynamics in particular behavioral contexts. Optogenetics provides rapid, bi-directional control of specific cell types within a region defined by the spatial profile of tissue illumination. Targeted light delivery to deep brain regions is typically achieved by 1–2 100–200-μm diameter optical fibers, which activate opsins expressed in a tissue volume extending several hundred microns axially from the fiber tip[42,57,58] (Figure 6C). Thus, depending on the geometry of underlying circuit dynamics, optogenetic experiments likely manipulate a volume that is either too small (in the case of widespread or distributed dynamics) or too large (in the case of sparse, localized dynamics). Moreover, most manipulations are conducted with limited knowledge of the spatial and temporal properties of the natural, underlying signals during the behavior of interest.

Our DA release measurements (Figures 4 and 5) underscore the importance of considering the true spatiotemporal dynamics of signaling; spatial profiles of modality-selective, stimulus-evoked DA release extended across 100s of microns to millimeters of space in 3 dimensions (Figure 4) and standard single-fiber (or large multi-fiber) optogenetic manipulations of DA terminals or midbrain cell-bodies could not differentially probe the impact of these distinct, widespread signals on behavior without significant over- or under-targeting. We have demonstrated, using DMD-guided light targeting of restricted locations through our fiber arrays, the ability to more precisely control the spatial spread and localization of optogenetic manipulations (Figures 6 and 7). Importantly, we are able to combine manipulations with large-scale simultaneous measurements in the same animal to better match the spatial scale, magnitude, and locations of light delivery with natural dynamics (Figure 6). Future applications of this technique could utilize the combinatorial illumination of multiple locations simultaneously to test the causal roles of distributed neural signals in behavior. Inversely, serial targeting of single, localized regions independently, within animal, could enable more precise localization of the critical circuit nodes that control specific behaviors (e.g., Figure 7). Our patterned illumination system also allows for flexible control over the timing of light delivery into individual fibers, allowing future manipulations that test the role of distributed endogenous signals with different timings (e.g., waves, Figure 5).

We have demonstrated the utility of our expanded multi-fiber array approach for targeted measurements and manipulations of neural signaling over a large three-dimensional volume within a single heterogeneous brain structure. However, most, if not all, complex behaviors likely involve rapid changes in neural signaling coordinated across many regions, and current techniques provide limited access to rapid large-scale signals, particularly across deep brain regions. Our multi-fiber approach can be easily extended in the future to measuring and manipulating population dynamics and function across multiple, arbitrarily spaced deep brain regions simultaneously without modifying the optical setup or basic implant design. Electrophysiological techniques for measuring cross-region activity, such as Neuropixels probes, although providing the advantage

of cellular resolution, do not offer genetic cell-type or neurotransmitter selectivity and are limited to sampling only from regions along the linear axis of the probe.[59] Our multi-fiber arrays can be used to identify where and how relevant task-related population dynamics are expressed, and then complementary electrophysiological (e.g., optotagging and Neuropixels) and cellular-resolution imaging can be applied to probe the cellular basis of the population signals in the targeted regions.

STAR★METHODS

Detailed methods are provided in the online version of this paper and include the following:

- KEY RESOURCES TABLE
- RESOURCE AVAILABILITY
  - Lead contact
  - Materials availability
  - Data and code availability
- EXPERIMENTAL MODEL AND STUDY PARTICIPANT DETAILS
  - Mice
- METHOD DETAILS
  - Multi-fiber array fabrication and calibration
  - Viral injections and array implantation
  - Micro-CT scanning and fiber localization
  - Possible alternative to CT-based localization
  - Immunohistology
  - Multi-color fiber array imaging
  - Targeted optogenetic stimulations
  - Freely moving imaging
  - Head-fixed behavior
- QUANTIFICATION AND STATISTICAL ANALYSIS
  - Velocity and acceleration
  - Multifiber photometry preprocessing
  - DA release to salient stimuli
  - DA release to optogenetic stimulation
  - Behavior response to optogenetic stimulation

Neuron
NeuroResource

REFERENCES

1. Allen, W.E., Kauvar, I.V., Chen, M.Z., Richman, E.B., Yang, S.J., Chan, K., Gradinaru, V., Deverman, B.E., Luo, L., and Deisseroth, K. (2017). Global representations of goal-directed behavior in distinct cell types of mouse neocortex. Neuron *94*, 891–907.e6.

2. Sofroniew, N.J., Flickinger, D., King, J., and Svoboda, K. (2016). A large field of view two-photon mesoscope with subcellular resolution for in vivo imaging. eLife *5*, e14472.

3. Barson, D., Hamodi, A.S., Shen, X., Lur, G., Constable, R.T., Cardin, J.A., Crair, M.C., and Higley, M.J. (2020). Simultaneous mesoscopic and two-photon imaging of neuronal activity in cortical circuits. Nat. Methods *17*, 107–113.

4. Cardin, J.A., Crair, M.C., and Higley, M.J. (2020). Mesoscopic imaging: shining a wide light on large-scale neural dynamics. Neuron *108*, 33–43.

5. Pinto, L., Rajan, K., DePasquale, B., Thiberge, S.Y., Tank, D.W., and Brody, C.D. (2019). Task-dependent changes in the large-scale dynamics and necessity of cortical regions. Neuron *104*, 810–824.e9.

6. Murphy, M.C., Chan, K.C., Kim, S.G., and Vazquez, A.L. (2018). Macroscale variation in resting-state neuronal activity and connectivity assessed by simultaneous calcium imaging, hemodynamic imaging and electrophysiology. NeuroImage *169*, 352–362.

7. Musall, S., Kaufman, M.T., Juavinett, A.L., Gluf, S., and Churchland, A.K. (2019). Single-trial neural dynamics are dominated by richly varied movements. Nat. Neurosci. *22*, 1677–1686.

8. Ghosh, K.K., Burns, L.D., Cocker, E.D., Nimmerjahn, A., Ziv, Y., Gamal, A.E., and Schnitzer, M.J. (2011). Miniaturized integration of a fluorescence microscope. Nat. Methods *8*, 871–878.

9. Ouzounov, D.G., Wang, T., Wang, M., Feng, D.D., Horton, N.G., Cruz-Hernández, J.C., Cheng, Y.T., Reimer, J., Tolias, A.S., Nishimura, N., et al. (2017). In vivo three-photon imaging of activity of GCaMP6-labeled neurons deep in intact mouse brain. Nat. Methods *14*, 388–390.

10. Yu, L., and Murari, K. (2021). Functional monitoring and imaging in deep brain structures. In Handbook of Neuroengineering, N.V. Thakor, ed. (Springer), pp. 1–32.

11. Adelsberger, H., Garaschuk, O., and Konnerth, A. (2005). Cortical calcium waves in resting newborn mice. Nat. Neurosci. *8*, 988–990.

12. Cui, G., Jun, S.B., Jin, X., Pham, M.D., Vogel, S.S., Lovinger, D.M., and Costa, R.M. (2013). Concurrent activation of striatal direct and indirect pathways during action initiation. Nature *494*, 238–242.

13. Pisanello, M., Pisano, F., Hyun, M., Maglie, E., Balena, A., De Vittorio, M., Sabatini, B.L., and Pisanello, F. (2019). The three-dimensional signal collection field for fiber photometry in brain tissue. Front. Neurosci. *13*, 82.

14. Sych, Y., Chernysheva, M., Sumanovski, L.T., and Helmchen, F. (2019). High-density multi-fiber photometry for studying large-scale brain circuit dynamics. Nat. Methods *16*, 553–560.

15. Kim, C.K., Yang, S.J., Pichamoorthy, N., Young, N.P., Kauvar, I., Jennings, J.H., Lerner, T.N., Berndt, A., Lee, S.Y., Ramakrishnan, C., et al. (2016). Simultaneous fast measurement of circuit dynamics at multiple sites across the mammalian brain. Nat. Methods *13*, 325–328.

16. Haber, S.N. (2016). Corticostriatal circuitry. Dialogues Clin. Neurosci. *18*, 7–21.

17. Thorn, C.A., Atallah, H., Howe, M., and Graybiel, A.M. (2010). Differential dynamics of activity changes in dorsolateral and dorsomedial striatal loops during learning. Neuron *66*, 781–795.

18. Lee, J., Wang, W., and Sabatini, B.L. (2020). Anatomically segregated basal ganglia pathways allow parallel behavioral modulation. Nat. Neurosci. *23*, 1388–1398.

19. Alexander, G.E., and Crutcher, M.D. (1990). Functional architecture of basal ganglia circuits: neural substrates of parallel processing. Trends Neurosci. *13*, 266–271.

20. Howe, M.W., and Dombeck, D.A. (2016). Rapid signalling in distinct dopaminergic axons during locomotion and reward. Nature *535*, 505–510.

21. Perkins, L.N., Semu, D., Shen, J., Boas, D.A., and Gardner, T.J. (2018). High-density microfibers as a potential optical interface to reach deep brain regions. J. Neural Eng. *15*, 066002.

22. Tai, D.C.S., Hooks, D.A., Harvey, J.D., Smaill, B.H., and Soeller, C. (2007). Illumination and fluorescence collection volumes for fiber optic probes in tissue. J. Biomed. Opt. *12*, 034033.

23. Engelbrecht, C.J., Göbel, W., and Helmchen, F. (2009). Enhanced fluorescence signal in nonlinear microscopy through supplementary fiber-optic light collection. Opt. Express *17*, 6421–6435.

24. Patriarchi, T., Cho, J.R., Merten, K., Howe, M.W., Marley, A., Xiong, W.H., Folk, R.W., Broussard, G.J., Liang, R., Jang, M.J., et al. (2018). Ultrafast neuronal imaging of dopamine dynamics with designed genetically encoded sensors. Science *360*, eaat4422.

25. Dana, H., Sun, Y., Mohar, B., Hulse, B.K., Kerlin, A.M., Hasseman, J.P., Tsegaye, G., Tsang, A., Wong, A., Patel, R., et al. (2019). High-performance calcium sensors for imaging activity in neuronal populations and microcompartments. Nat. Methods *16*, 649–657.

26. Jing, M., Li, Y., Zeng, J., Huang, P., Skirzewski, M., Kljakic, O., Peng, W., Qian, T., Tan, K., Zou, J., et al. (2020). An optimized acetylcholine sensor for monitoring in vivo cholinergic activity. Nat. Methods *17*, 1139–1146.

27. Dombeck, D.A., Harvey, C.D., Tian, L., Looger, L.L., and Tank, D.W. (2010). Functional imaging of hippocampal place cells at cellular resolution during virtual navigation. Nat. Neurosci. *13*, 1433–1440.

28. Legaria, A.A., Matikainen-Ankney, B.A., Yang, B., Ahanonu, B., Licholai, J.A., Parker, J.G., and Kravitz, A.V. (2022). Fiber photometry in striatum reflects primarily nonsomatic changes in calcium. Nat. Neurosci. *25*, 1124–1128.

29. Markowitz, J.E., Gillis, W.F., Beron, C.C., Neufeld, S.Q., Robertson, K., Bhagat, N.D., Peterson, R.E., Peterson, E., Hyun, M., Linderman, S.W., et al. (2018). The striatum organizes 3D behavior via moment-to-moment action selection. Cell *174*, 44–58.e17.

30. Perkins, L.N., Devor, A., Gardner, T.J., and Boas, D.A. (2018). Extracting individual neural activity recorded through splayed optical microfibers. Neurophotonics *5*, 045009.

31. Metscher, B.D. (2009). MicroCT for developmental biology: A versatile tool for high-contrast 3D imaging at histological resolutions. Dev. Dyn. *238*, 632–640.

32. Wang, Q., Ding, S.L., Li, Y., Royall, J., Feng, D., Lesnar, P., Graddis, N., Naeemi, M., Facer, B., Ho, A., et al. (2020). The Allen Mouse Brain Common coordinate framework: A 3D reference atlas. Cell *181*, 936–953.e20.

33. Fedorov, A., Beichel, R., Kalpathy-Cramer, J., Finet, J., Fillion-Robin, J.C., Pujol, S., Bauer, C., Jennings, D., Fennessy, F., Sonka, M., et al. (2012). 3D Slicer as an image computing platform for the Quantitative Imaging Network. Magn. Reson. Imaging *30*, 1323–1341.

34. Liberti, W.A., Markowitz, J.E., Perkins, L.N., Liberti, D.C., Leman, D.P., Guitchounts, G., Velho, T., Kotton, D.N., Lois, C., and Gardner, T.J. (2016). Unstable neurons underlie a stable learned behavior. Nat. Neurosci. *19*, 1665–1671.

35. Liberti, W.A., Perkins, L.N., Leman, D.P., and Gardner, T.J. (2017). An open source, wireless capable miniature microscope system. J. Neural Eng. *14*, 045001.

36. Schultz, W. (2007). Multiple dopamine functions at different time courses. Annu. Rev. Neurosci. *30*, 259–288.

37. Redgrave, P., and Gurney, K. (2006). The short-latency dopamine signal: a role in discovering novel actions? Nat. Rev. Neurosci. *7*, 967–975.

38. Steinfels, G.F., Heym, J., Strecker, R.E., and Jacobs, B.L. (1983). Behavioral correlates of dopaminergic unit activity in freely moving cats. Brain Res. *258*, 217–228.

39. Menegas, W., Babayan, B.M., Uchida, N., and Watabe-Uchida, M. (2017). Opposite initialization to novel cues in dopamine signaling in ventral and posterior striatum in mice. eLife *6*, e21886.

40. Hamid, A.A., Frank, M.J., and Moore, C.I. (2021). Wave-like dopamine dynamics as a mechanism for spatiotemporal credit assignment. Cell *184*, 2733–2749.e16.

41. Sun, F., Zhou, J., Dai, B., Qian, T., Zeng, J., Li, X., Zhuo, Y., Zhang, Y., Wang, Y., Qian, C., et al. (2020). Next-generation GRAB sensors for monitoring dopaminergic activity in vivo. Nat. Methods *17*, 1156–1166.

42. Yona, G., Meitav, N., Kahn, I., and Shoham, S. (2016). Realistic numerical and analytical modeling of light scattering in brain tissue for optogenetic applications(1,2,3). eNeuro *3*, 0059–15.2015.

43. Zhuo, Y., Luo, B., Yi, X., Dong, H., Miao, X., Wan, J., Williams, J.T., Campbell, M.G., Cai, R., Qian, T., et al. (2023). Improved green and red GRAB sensors for monitoring dopaminergic activity in vivo. Published online November 30, 2023. Nat. Methods.

44. Matsuda, W., Furuta, T., Nakamura, K.C., Hioki, H., Fujiyama, F., Arai, R., and Kaneko, T. (2009). Single nigrostriatal dopaminergic neurons form widely spread and highly dense axonal arborizations in the neostriatum. J. Neurosci. *29*, 444–453.

45. Hintiryan, H., Foster, N.N., Bowman, I., Bay, M., Song, M.Y., Gou, L., Yamashita, S., Bienkowski, M.S., Zingg, B., Zhu, M., et al. (2016). The mouse cortico-striatal projectome. Nat. Neurosci. *19*, 1100–1114.

46. Hunnicutt, B.J., Jongbloets, B.C., Birdsong, W.T., Gertz, K.J., Zhong, H., and Mao, T. (2016). A comprehensive excitatory input map of the striatum reveals novel functional organization. eLife *5*, e19103.

47. Mathis, A., Mamidanna, P., Cury, K.M., Abe, T., Murthy, V.N., Mathis, M.W., and Bethge, M. (2018). DeepLabCut: markerless pose estimation of user-defined body parts with deep learning. Nat. Neurosci. *21*, 1281–1289.

48. Nath, T., Mathis, A., Chen, A.C., Patel, A., Bethge, M., and Mathis, M.W. (2019). Using DeepLabCut for 3D markerless pose estimation across species and behaviors. Nat. Protoc. *14*, 2152–2176.

49. Menegas, W., Akiti, K., Amo, R., Uchida, N., and Watabe-Uchida, M. (2018). Dopamine neurons projecting to the posterior striatum reinforce avoidance of threatening stimuli. Nat. Neurosci. *21*, 1421–1430.

50. Tsutsui-Kimura, I., Uchida, N., and Watabe-Uchida, M. (2022). Dynamical management of potential threats regulated by dopamine and direct- and indirect-pathway neurons in the tail of the striatum. Preprint at bioRxiv.

51. Jin, S.W., and Lee, I. (2021). Differential encoding of place value between the dorsal and intermediate hippocampus. Curr. Biol. *31*, 3053–3072.e5.

52. Collins, A.L., and Saunders, B.T. (2020). Heterogeneity in striatal dopamine circuits: form and function in dynamic reward seeking. J. Neurosci. Res. *98*, 1046–1069.

53. Fanselow, M.S., and Dong, H.W. (2010). Are the dorsal and ventral hippocampus functionally distinct structures? Neuron *65*, 7–19.

54. Lubenov, E.V., and Siapas, A.G. (2009). Hippocampal theta oscillations are travelling waves. Nature *459*, 534–539.

55. Leybaert, L., and Sanderson, M.J. (2012). Intercellular Ca(2+) waves: mechanisms and function. Physiol. Rev. *92*, 1359–1392.

56. Berdyyeva, T.K., Frady, E.P., Nassi, J.J., Aluisio, L., Cherkas, Y., Otte, S., Wyatt, R.M., Dugovic, C., Ghosh, K.K., Schnitzer, M.J., et al. (2016). Direct imaging of hippocampal epileptiform calcium motifs following kainic acid administration in freely behaving mice. Front. Neurosci. *10*, 53.

57. Aravanis, A.M., Wang, L.P., Zhang, F., Meltzer, L.A., Mogri, M.Z., Schneider, M.B., and Deisseroth, K. (2007). An optical neural interface: *in vivo* control of rodent motor cortex with integrated fiberoptic and optogenetic technology. J. Neural Eng. *4*, S143–S156.

58. Spagnolo, B., Peixoto, R.T., Sileo, L., Pisanello, M., Pisano, F., Assad, J.A., Sabatini, B.L., Vittorio, M.D., and Pisanello, F. (2020). Integrated tapered fibertrode for simultaneous control and readout of neural activity over small brain volumes with reduced light-induced artefacts. Preprint at bioRxiv.

59. Jun, J.J., Steinmetz, N.A., Siegle, J.H., Denman, D.J., Bauza, M., Barbarits, B., Lee, A.K., Anastassiou, C.A., Andrei, A., Aydın, Ç., et al. (2017). Fully integrated silicon probes for high-density recording of neural activity. Nature *551*, 232–236.

60. Dana, H., Mohar, B., Sun, Y., Narayan, S., Gordus, A., Hasseman, J.P., Tsegaye, G., Holt, G.T., Hu, A., Walpita, D., et al. (2016). Sensitive red protein calcium indicators for imaging neural activity. eLife *5*, e12727.

61. Schindelin, J., Arganda-Carreras, I., Frise, E., Kaynig, V., Longair, M., Pietzsch, T., Preibisch, S., Rueden, C., Saalfeld, S., Schmid, B., et al. (2012). Fiji: an open-source platform for biological-image analysis. Nat. Methods *9*, 676–682.

62. UCLA Miniscope. Main page. http://miniscope.org/index.php/Main_Page.

63. Deverman, B.E., Pravdo, P.L., Simpson, B.P., Kumar, S.R., Chan, K.Y., Banerjee, A., Wu, W.L., Yang, B., Huber, N., Pasca, S.P., et al. (2016). Cre-dependent selection yields AAV variants for widespread gene transfer to the adult brain. Nat. Biotechnol. *34*, 204–209.

64. Degenhardt, K., Wright, A.C., Horng, D., Padmanabhan, A., and Epstein, J.A. (2010). Rapid 3D phenotyping of cardiovascular development in mouse embryos by micro-CT with iodine staining. Circ. Cardiovasc. Imaging *3*, 314–322.

65. Sergejeva, M., Papp, E.A., Bakker, R., Gaudnek, M.A., Okamura-Oho, Y., Boline, J., Bjaalie, J.G., and Hess, A. (2015). Anatomical landmarks for registration of experimental image data to volumetric rodent brain atlasing templates. J. Neurosci. Methods *240*, 161–169.

66. Chon, U., Vanselow, D.J., Cheng, K.C., and Kim, Y. (2019). Enhanced and unified anatomical labeling for a common mouse brain atlas. Nat. Commun. *10*, 5067.

67. Allen Brain Map Community Forum (2019). Why doesn't the 3D Mouse Brain Atlas have Bregma coordinates? https://community.brain-map.org/t/why-doesnt-the-3d-mouse-brain-atlas-have-bregma-coordinates/158.

68. Shamash, P., Carandini, M., Harris, K., and Steinmetz, N. (2018). A tool for analyzing electrode tracks from slice histology. Preprint at bioRxiv.

69. Hopkins, T.M., Heilman, A.M., Liggett, J.A., LaSance, K., Little, K.J., Hom, D.B., Minteer, D.M., Marra, K.G., and Pixley, S.K. (2015). Combining

micro-computed tomography with histology to analyze biomedical implants for peripheral nerve repair. J. Neurosci. Methods *255*, 122–130.

70. Azimipour, M., Baumgartner, R., Liu, Y., Jacques, S.L., Eliceiri, K., and Pashaie, R. (2014). Extraction of optical properties and prediction of light distribution in rat brain tissue. J. Biomed. Opt. *19*, 75001.

71. Al-Juboori, S.I., Dondzillo, A., Stubblefield, E.A., Felsen, G., Lei, T.C., and Klug, A. (2013). Light scattering properties vary across different regions of the adult mouse brain. PLoS One *8*, e67626.

72. Zhang, F., Wang, L.P., Boyden, E.S., and Deisseroth, K. (2006). Channelrhodopsin-2 and optical control of excitable cells. Nat. Methods *3*, 785–792.

73. Grossman, N., Simiaki, V., Martinet, C., Toumazou, C., Schultz, S.R., and Nikolic, K. (2013). The spatial pattern of light determines the kinetics and modulates backpropagation of optogenetic action potentials. J. Comput. Neurosci. *34*, 477–488.

74. Pnevmatikakis, E.A., and Giovannucci, A. (2017). NoRMCorre: An online algorithm for piecewise rigid motion correction of calcium imaging data. J. Neurosci. Methods *291*, 83–94.

75. Garland, T., Gleeson, T.T., Aronovitz, B.A., Richardson, C.S., and Dohm, M.R. (1995). Maximal sprint speeds and muscle fiber composition of wild and laboratory house mice. Physiol. Behav. *58*, 869–876.

STAR★METHODS

KEY RESOURCES TABLE

REAGENT or RESOURCE	SOURCE	IDENTIFIER
Antibodies		
Normal Goat Serum (Invitrogen)	ThermoFisher	Cat#31873; RRID: AB_2532167
Bovine Serum Albumin	Sigma-Aldrich	Cat#A3059
VECTASHIELD® PLUS Antifade Mounting Medium with DAPI	Vector Laboratories	Cat#H-2000
GFP Polyclonal Antibody	ThermoFisher	Cat#A10262; RRID: AB_2534023; Lot#2622405
Goat anti-Chicken IgY (H+L) Secondary Antibody, Alexa Fluor™ 488	Thermofisher	Cat#A-11039; RRID: AB_2534096; Lot# 2566343
NeuN antibody	Synaptic Systems	Cat#266 044; RRID: AB_2620156; Lot#7-58
Goat anti-Guinea Pig IgG (H+L) Highly Cross-Adsorbed Secondary Antibody, Alexa Fluor™ 647	ThermoFisher	Cat#A-21450; RRID: AB_2735091; Lot#2633525
Bacterial and virus strains		
pAAV-CAG-dLight1.3b	Addgene; Patriarchi et al.[24]	Cat#125560-AAV5; RRID:Addgene_125560
pGP-AAV-syn-FLEX-jGCaMP7f-WPRE	Addgene; Dana et al.[25]	Cat#104492-AAV1; RRID:Addgene_104492
AAV9-hSyn-Ach3.0	WZ Biosciences	Cat#YL001003-AV9-PUB; RRID: Addgene_121922
pAAV-syn-FLEX-NES-jRGECO1a-WPRE-SV40	Addgene; Dana et al.[60]	Cat#100853; RRID:Addgene_100853
pAAV-hSyn-rDA3m-WPRE-pA	Biohippo; Zhuo et al.[43]	Cat#: BHV12400545-6
pAAV-CAG-tdTomato (codon diversified-AAV1)	Addgene	Cat#59462-AAV1; RRID:Addgene_59462
pAAV-EF1a-double floxed hChR2(H134R)EYFP-WPRE-HGHpA	Addgene	Cat#20298-AAV1; RRID:Addgene_20298
Deposited data		
original data and analysis code	this paper	Zenodo: https://doi.org/10.5281/zenodo.10272873
Experimental models: Organisms/strains		
Mice: C57BL/6J	The Jackson Laboratory	RRID:IMSR_JAX:000664
Mice: DAT-IRES-cre	The Jackson Laboratory	RRID:IMSR_JAX:006660
Mice: D1-Cre (C57BL/6J)	The Jackson Laboratory	RRID: MMRRC_037156-JAX
Software and algorithms		
FIJI/ImageJ	Schindelin et al.[61]	RRID:SCR_002285; https://imagej.net/software/fiji/
MATLAB 2020b	Mathworks	RRID:SCR_001622; https://www.mathworks.com/products/matlab.html
3D Slicer	Fedorov et al.[33]	RRID:SCR_005619; https://www.slicer.org/
HCImage	Hamamatsu	RRID:SCR_015041; https://hcimage.com/
NormCorre	Pnevmatikakis & Giovannucci, 2017[62]	https://github.com/flatironinstitute/NoRMCorre
Allen Mouse Brain Common Coordinate Framework	Wang et al.[32]	RRID:SCR_020999; https://atlas.brain-map.org/
Polyscan 2		https://www.mightexbio.com/products/software/polyscan3-2/
Other		
Lugol's solution	Carolina Sciences	Cat#872795
Sodium Thiosulfate, Anhydrous	Carolina Sciences	Cat#892020

RESOURCE AVAILABILITY

Lead contact
Further information and requests for resources should be directed to the lead contact, Mark W. Howe (mwhowe@bu.edu).

Materials availability
This study did not generate new unique reagents.

Data and code availability
All original code used to preprocess and analyze the data and generate the figures has been deposited at Zenodo and is publicly available as of the date of publication (Zenodo: https://doi.org/10.5281/zenodo.1027287 43); DOI(s) are listed in the key resources table. Public use versions of our pipeline and code for imaging data preprocessing and CT-based fiber localization are available on Github: https://github.com/HoweLab/MultifiberProcessing and https://github.com/HoweLab/MultifiberLocalization, respectively.

EXPERIMENTAL MODEL AND STUDY PARTICIPANT DETAILS

Mice
C57BL6 (6 males, 6 females; Figures 1D, 2, 3C, 4, 5, S1, S2, and S3–S6), DAT-cre (1 male, 3 females; Figures 6 and S7A, Jackson Labs, strain #006660), and Drd1-cre (1 male, 2 females; Figures 1C, 3A, 3B, 7, S2D–S2F, S7B, and S7C Jackson labs, strain #030329) ages 11 to 31 weeks, were used. Mice were housed under a 12h light-dark cycle (light on 9pm-9am). Unimplanted mice were group-housed 2-5 per cage; upon implantation, mice were housed singly. Experiments were performed during the dark cycle. Animals had free access to food and water, except in cases when the animal was water scheduled. All studies and procedures were approved by the Boston University Institutional Animal Care and Use Committee.

METHOD DETAILS

Multi-fiber array fabrication and calibration
Multi-fiber arrays were fabricated in-house to enable large scale measurements across deep brain volumes. Fibers (Fiber Optics Tech) had an outer diameter of either 37μm (34μm core, 3μm cladding) or 50μm (46μm core, 4μm cladding) with 0.66NA. Bare fibers were cut into pieces ($\sim$3cm) then mounted under a microscope into 55-60μm diameter holes in a custom 3D printed grid (Figure 1A, 3mm W x 5mm L, Boston Micro Fabrication), measured under a dissection microscope to target a particular depth beneath the grid, and secured in place with UV glue (Norland Optical Adhesive 61). Each array contained between 30 and 103 fibers separated by a minimum of 220μm radially and 250μm axially. Separation was calculated to achieve maximal coverage of the striatum volume with no overlap in the collection fields of individual fibers.[13] Fibers were cut with a fiber scribe, and the distal ends were inspected to ensure a uniform cut, and re-cut as necessary. Distal ends were then glued inside an $\sim$1cm section of polyimide tube (0.8-1.3mm diameter, MicroLumen) then cut with a fresh razorblade. The bundled fibers inside the tube were then polished on fine grained polishing paper (ThorLabs,polished first with 6 μm, followed by 3 μm) to create a smooth, uniform fiber bundle surface for imaging (Figure 1B inset, and 2A). A larger diameter post was mounted on one side of the plastic grid to facilitate holding during implantation (Figure 1A).

Prior to implantation, a calibration procedure was performed on the fabricated fiber arrays to match each fiber on the implanted side to a location on the bundle surface. To do this, distal (implanted) ends were illuminated with a flashlight, and transmitted light was imaged on the bundle surface. A sequence of illuminations was performed with different rows and columns covered, allowing each fiber on the imaging surface to be mapped to a specific row and column of the grid and distal fiber ends (Figure 2A).

For the online protocol, see protocols.io: https://doi.org/10.17504/protocols.io.bp2l6xyrklqe/v1.

Viral injections and array implantation
Mice were injected with AAVs to express genetically encoded proteins for optical measurements and manipulations (see Table S1). Mice were anesthetized under isoflurane (1-3%) and placed in a stereotaxic frame. A large craniotomy was performed with a surgical drill (Midwest Tradition 790044, Avtec Dental RMWT) to expose the cortical surface above the striatum. For striatum expression, virus was injected stereotaxically through a pulled glass pipette (diameter 30-50μm) at 10-40 total locations (200-800nL at each location at a rate $\sim$ 100 nL/min) chosen to maximize overlap with fiber positions. Transgenic mice with endogenous expression of fluorescent sensors or viruses that drive a greater spread of expression[63] may be used to eliminate the need for multiple viral injections and minimize tissue disruption and inflammation. Injections were targeted to the midbrain for the stimulation experiment (Figure 6) at 4 sites relative to bregma: AP = -3.05, ML = 0.6, DV = -4.6 and DV = -4.25; AP = -3.5, ML = 1.25, DV = -3.9 and DV = -4.5. Injections to target midbrain DA neurons for the dual-wavelength recordings (Figure S2C) were performed 3.07mm caudal to the bregma at four sites: ML = 0.5mm, DV =-4.00 mm and -4.25 mm, ML = 1mm, DV = -4.125mm and ML = 1.5 mm, DV = -3.8 mm below the dura, 200-400nL at each site at a rate $\sim$ 100 nL/min. The fiber array was then mounted in the stereotaxic and slowly lowered into position until one side of the grid contacted the skull surface. Precise targeting of the array and rigid placement into the stereotaxic is essential to avoid misplacement of fibers (which may result in tissue distortion) and tissue damage caused by lateral movements of the fibers. A thin layer of

Kwik-Sil (WPI) was applied to seal off the exposed edges of the craniotomy, and then Metabond (Parkell) was used to secure the plastic frame to the skull. After this initial layer of Metabond solidified, a metal headplate and ring[20,27] (Atlas Tool and Die Works) were secured to the skull with Metabond and the surface covered with a layer of blackened Metabond (carbon powder, Sigma). Finally, a small cylindrical plastic protective cap cut to extend just above the fiber bundle end was secured around the bundle and covered on the inside surface with blackened Metabond. Behavioral habituation began 1 or more weeks after surgery, and neural data acquisition began 3-5 weeks after injection and implant surgery.

For the online protocol, see protocols.io: https://doi.org/10.17504/protocols.io.bp2l6xyrklqe/v1.

Micro-CT scanning and fiber localization

After completion of neural recording and behavioral experiments, mice were injected intraperitoneally with 400-500 mg/kg Euthasol (Covetrus Euthanasia III), and then perfused transcardially with 20mL 1% phosphate buffered saline (PBS, Fisher), followed by 20mL 4% paraformaldehyde in 1% PBS. After perfusion and decapitation, the lower jaw and front of the skull were removed in order to allow diffusion of solution into the brain while still keeping the implant intact. The brain was soaked in the 4% paraformaldehyde solution for 24h, rinsed three times with 1% PBS, and then transferred to a diluted Lugol's solution, to provide tissue contrast for computerized tomography (CT) scanning.[31] The Lugol solution was prepared by diluting 10mL 100% Lugol's Solution (Carolina, 10% potassium iodide, 5% iodine) with 30mL deionized water, a dilution chosen to be approximately isotonic to biological tissues.[64] Initially, samples were soaked in this diluted Lugol's solution in a foil-wrapped 50mL conical centrifuge tube on an orbital shaker plate for 10-14 days. We have more recently found that using 4 oz specimen cups instead of the 50mL conical centrifuge tubes enables better diffusion of the Lugol's solution, and adequate contrast can be achieved in three to four days. After soaking, the skulls were rinsed three times with 1% PBS, secured in a modified centrifuge tube, and imaged in a micro-CT scanner (Zeiss Xradia Versa 520, a core instrument of the Boston University Micro-CT and X-ray Microscopy Imaging Facility) with the following parameters: 140kV, 10W, HE1 filter, 0.4X objective, 2s exposure time, 1001 projections, 12-micron voxel size.

The CT was then registered to the Allen Mouse Brain Common Coordinate Framework 3D 10-micron reference atlas[32] to bring individual mice into a common coordinate system, and then fibers were identified and mapped from the recording tip up to the grid. To register the CT to the atlas, the 3D image was first oriented coronally, using 50-150 experimenter-identified points along the midsagittal plane, and a rough estimation of the anterior-posterior tilt of the brain. Then, previously-established landmarks,[65] were manually identified and marked on the CT scan using the Name Landmarks and Register plugin in FIJI/ImageJ.[61] A reference set of these landmarks was established by taking the mean location of the landmarks independently identified by seven lab members on the atlas. All subsequent steps were carried out in MATLAB (Mathworks, version 2020b) using a combination of existing MATLAB functions and custom lab-written functions and GUIs. The landmarks, separated into lateralized landmarks and midsagittal landmarks, were then used to register the CT to the reference atlas in a 3-step process. First, the midsagittal landmarks, in combination with the 50-150 previously identified midsagittal points, were used to re-establish the midsagittal plane, and the medial-lateral dimension of the CT was rescaled to match the atlas using the distance between the lateralized landmarks and midsagittal plane. Next, a rigid registration based on the midsagittal landmarks established a coarse anterior-posterior and dorsal-ventral alignment. And finally, the anterior-posterior and dorsal-ventral alignment was refined using an affine registration based on the midsagittal landmarks. The registration was then verified and manually refined using a lab-developed GUI.

Fibers were then identified and localized in a series of semi-automated steps. Fibers are very bright on the CT scan (Figures 2B and 2C) so are easy to identify automatically based on intensity. First, the tops of the fibers were aligned and assigned to the grid (which was previously mapped to the imaging surface, Figure 2A). A dorsal slice was chosen where the row and column organization of the fibers could be clearly visualized. The fiber cross sections were automatically detected using the MATLAB functions *adaptthresh* and *imbinarize* to binarize the image, and then *bwconncomp* with a connectivity of 4 to find connected components, i.e., each fiber. The fibers were then automatically assigned to the grid based on spacing and input grid design, and the assignment was manually checked and refined as necessary.

Next, on an axial max projection of the CT scan, a polygon was drawn around the fibers to restrict fiber identification to this area. The CT scan was binarized, using *adaptthresh* and *imbinarize*, as before, within the defined area on each axial slice. The resulting binarized volume was then segmented into 3D connected components using *bwconncomp*, with a connectivity of 26. Only components connected to one of the identified, grid-assigned, fiber tops were considered fibers. In some cases when fibers crossed, they were lumped together into the same 3D connected component, and these cases were easily identified by virtue of being connected to multiple fiber tops. These "multifibers" were separated using watershed segmentation (*watershed* function in MATLAB) on sequential axial slices to separate the touching fibers. For each of the fiber tops in the "multifiber", a line was established from the centers (found using the *regionprops* function in MATLAB) of each of the fiber's cross sections in the first 10 slices. Given the voxel size, and fiber spacing of at least 220 microns in either the medial-lateral or anterior-posterior directions, it is not possible for them to cross within these first 10 axial slices. Continuing to move ventrally, watershed-separated fiber cross sections were assigned to each "fiber line" based on best fit, and with each subsequently assigned section, the line was iteratively updated. The resulting separated "multifiber" was verified by the experimenter and refined as necessary. Once there was a 1:1 mapping between fiber tops and fiber bottoms, the fiber identification step was complete, and the recording location was assigned to the center of the most ventral cross-section slice of the fiber. Anatomical labels were automatically assigned to each fiber recording location using available segmentations of the Allen

Mouse Brain Common Coordinate Framework 3D 10-micron reference atlas.[32,66] Assigned locations were then manually verified and anatomical labels were refined in borderline cases where necessary.

For approximate conversion of recording locations in 3D atlas space to a Bregma-centered coordinate system, we converted distance in voxels (isotropic 10 microns) to distance from Bregma. The medial-lateral coordinate of Bregma was defined as the midsagittal plane. The anterior-posterior coordinate of Bregma was taken from an open-source atlas that merged the Franklin-Paxinos atlas into the Allen Mouse Brain Common Coordinate Framework 3D atlas.[66] The dorsal-ventral coordinate of Bregma was estimated by taking the average of repeated identification of landmarks along the midsagittal line on the AP=0mm coronal slice on both the Allen Mouse Brain Common Coordinate Framework 3D atlas and the Franklin Paxinos atlas, and then from those points, estimating the 0 point on the Allen Mouse Brain atlas. We note that the Allen Mouse Brain Common Coordinate Framework 3D atlas does not provide Bregma coordinates due to methodological considerations.[67] When provided, our Bregma-centric coordinates are for purposes of approximate reference for comparison with other atlases.

For the online protocol, see protocols.io: https://doi.org/10.17504/protocols.io.bp2l6xyrklqe/v1.

Possible alternative to CT-based localization

The smaller diameter of the fibers makes them more flexible than larger fibers, and as a result, implantation may change the spatial relationship between the tips and some fibers may even end up crossing (Figures 1E and S3). It is for this reason that we rely on the 3D CT scan of the implanted brain for unambiguous localization of these densely arranged fibers. Nonetheless, it may be possible for those without access to a micro-CT scanner to localize fibers using more conventional histological methods. In our histological slices taken after the CT scan protocol (i.e., after soaking 24h in PFA, 3-4 days in Lugol's solution, and then in 4-6 days in sodium thiosulfate, see Immunohistology methods section), tracks were visible (see Figures S1 and S7C), and resources exist[68] that facilitate registration of histological slices with the same reference atlas we have used. It might require using fewer fibers and increasing the spacing between them to minimize the chances of crossing fibers. Furthermore, since the track of a single fiber is unlikely to be contained in a single slice (see Figure S1, where full-length tracks are not in the same plane as the slice), in order to accurately localize the tip, users might need to follow the fiber track across multiple slices. A potential avenue might be to reconstruct the implanted brain volume from sequential slices into a 3D image, and then adapt our code to localize fibers in the reconstructed 3D image.

Immunohistology

In preparation for immunohistology, Lugol's solution was removed from brain tissue after CT imaging by soaking the implanted brains in a solution of 5% sodium thiosulfate (STS, Carolina) in 1% PBS for 4-6 days.[69] The implant was then removed, the brain returned to the STS solution for one hour, and then moved to a solution of 30-40% sucrose in PBS. Once the brains sank, coronal sections (50 μm) were sliced with a cryostat (Leica CM3050 S) and transferred to PBS for storage. To stain for dLight1.3b (Figure S1H) or ChR2 expression (Figure S7C), sections were then blocked and treated in a 5% normal goat serum (NGS) and 0.2% PBS triton (Sigma Aldrich) solution (PBST). Treated sections were then incubated for 24-48 hours at 4°C in 5% NGS, 0.2% triton, and a GFP primary antibody (chicken polyclonal antibody; 1:1000, ThermoFisher Scientific, No. A10262). Slices were then washed, and incubated for 2 hours at room temperature in 5% NGS, 0.2% PBST, and an Alexa 488 secondary antibody (goat anti-chicken; 1:200, ThermoFisher Scientific, No.A-11039). For neuronal staining (Figures S1A–S1G), sections then blocked and treated in a 5% bovine serum albumin (BSA) and 0.2% PBS triton (Sigma Aldrich) solution (PBST). Treated sections were then incubated for 24-48 hours at 4°C in 5% BSA, 0.2% triton, and a NeuN primary antibody (guinea pig antibody; 1:500, Synaptic Systems, 266 004). Slices were then washed, and incubated for 2 hours at room temperature in 5% BSA, 0.2% PBST, and an Alexa 647 secondary antibody (goat anti-guinea pig; 1:200, ThermoFisher Scientific, No. A-21450). Finally, stained sections were mounted onto glass slides using Vectashield Mounting Medium with DAPI (Vector Laboratories, H-2000) and confocal images were acquired with a Zeiss LSM 800. While this protocol was adequate to resolve expression, it may be possible to further optimize the destaining, cryoprotection, and slicing procedures for more optimal immunohistology results.

For quantification of neuronal density in the NeuN-labeled sections (Figures S1A–S1G), images of striatum (implanted and unimplanted) were taken of DAPI and NeuN at 20x magnification. A single image was generated by multiplying these images together to emphasize co-stained pixels to eliminate any pixels that were artifactually bright in a single channel. The resulting image was adaptively thresholded and binarized using Otsu's method via MATLAB's *graythresh*, and then neuron centers were identified via *imfindcircles* using a radius range of 5-30 pixels.

Fibers are unlabeled (dark) on these images, and were automatically detected via an intensity threshold, and then manually rejected or refined based on the CT. The shape of the fiber track and the CT were used to determine whether the visible fiber was the tip or not. The striatum border was manually traced on the acquired images, and only pixels within the striatum were considered for all calculations. To quantify the neuron density below fiber tips at increasing depths, neuron counts were calculated in 50-micron boxes beginning just ventral to the tip, and then slid incrementally ventral in 10-micron steps (Figure S1D). These counts were then converted to density ($1/mm^2$). For comparison, 10 thousand 50-micron boxes were randomly sampled from unimplanted striatum images, generating a distribution. To quantify the neuron density between neighboring fibers, fibers were first determined to be a pair if they were next to each other on the slice and overlapped along the dorsal/ventral axis. The inter-fiber area was defined as the inner medial/lateral edges (also a measure of inter-fiber distance) and outer dorsal/ventral points (see Figure S1D). In cases where one of the fibers was a tip, its ventral most point defined the ventral extent of the inter-fiber area. The neuron count from within this

area was then converted to density (1/mm^2). For comparison, neuron density was calculated for entire unimplanted striatal regions of interest.

For the online protocol, see protocols.io: https://doi.org/10.17504/protocols.io.bp2l6xyrklqe/v1.

Multi-color fiber array imaging

Fiber bundle imaging for head-fixed experiments was performed with a custom microscope mounted on a 4' x 8' x 12'' vibration isolation table (Newport, Figure 1B). Excitation light (470nm, 405nm, 415nm, and 570nm) for fluorescent sensors was provided by high-power Solis LEDs (Thor labs, No. SOLIS-470C, SOLIS-405C, SOLIS-415C, SOLIS-570C) which were combined using a series of two dichroic filters (Chroma No. ZT532rdc and 405rdc). Light from the LEDs was filtered (Chroma No. ET405/10, ET555/25, ET473/24) and coupled into a liquid light guide (Newport No. 77632) with lenses (f = 60mm and 30mm, Thor labs No. LA1401-A and LA1805) and a collimating beam probe (Newport No. 76600). The liquid light guide was coupled into a filter cube on the microscope and excitation light was reflected into the back aperture of the microscope objective (10x, 0.3NA, Olympus No. UPLFLN10X2) by a dichroic beam-splitter (Chroma No. 59009bs). Light power measured at the focal plane of the objective was set to 65-90 mW which produced ~1.6-2 mW/mm^2 power at the fiber tips. Fluorescence from the fiber bundle was collected by the objective then passed through the dichroic beam-splitter used to direct the excitation light. A second dichroic (Chroma, No. 532rdc) reflected green and passed red fluorescence, and bandpass filters for red and green (Chroma, No. 570lp and 525/50m respectively) blocked residual excitation light and autofluorescence. A tube lens in each path (Thor labs, No TTL165-A) focused emission light onto the CMOS sensors of the cameras to form an image of the fiber bundle (Hamamatsu, Orca Fusion BT Gen III). The microscope was attached to a micromanipulator (Newport No. 9067-XYZ-R) to allow fine manual focusing and mounted on a rotatable arm extending over the head-fixation setup to allow for coarse positioning of the objective over the mouse.

Imaging data was acquired using HCImage Live (Hamamatsu). Single wavelength excitation and emission was performed with continuous, internally triggered imaging at 30Hz. For dual-wavelength excitation and emission, two LEDs were triggered by 5V digital TTL pulses which alternated at either 11Hz (33ms exposure) or 18Hz (20ms exposure). To synchronize each LED with the appropriate camera (e.g. 470nm LED excitation to green emission camera), the LED trigger pulses were sent in parallel (and decreased to 3.3V via a pulldown circuit) to the cameras to trigger exposure timing. The timing and duration of digital pulses were controlled by custom MATLAB software through a programmable digital acquisition card ("NIDAQ", National Instruments PCIe 6343). Voltage pulses were sent back from the cameras to the NIDAQ card after exposure of each frame to confirm proper camera triggering and to align imaging data with behavior data (see below).

For the online protocol, see protocols.io: https://doi.org/10.17504/protocols.io.bp2l6xyrklqe/v1.

Targeted optogenetic stimulations

To couple light into individual optical fibers in our array for targeted optogenetic manipulations, simultaneously with imaging (Figures 6 and 7), we integrated a programmable digital mirror device (DMD, Mightex Polygon1000 Pattern Illuminator DSI-K3-L20) into the light path of our imaging microscope (Figure 6A). Excitation light was provided by a 3.2W, 465nm laser (Mightex, LSR-040-0465), which was coupled to the DMD with an optical fiber. Light from the DMD was coupled into the objective path by a dichroic (Chroma 570lpxr). 570nm excitation and emission filters (see 'Multi-color fiber array imaging' above and Figure 6A) enabled simultaneous imaging of red fluorophores during stimulation.

Control of light patterning and stimulation parameters was achieved with PolyScan2 control software (Mightex) and custom MATLAB functions. A calibration step was performed prior to stimulations to align the camera view with the PolyScan2 software, allowing us to design patterns of circular light (~40μm diameter for each spot) to target individual fibers (Figures 6A, 6B, and 6D). Transmission efficiency through 50μm diameter fibers in our arrays was calculated at approximately 39% based on comparisons between power at the objective and transmitted light through individual fibers. For stimulations of dopamine release (Figure 6), a light spot of ~750 μW (measured at the objective) was used, resulting in an estimated power density of 175 mW/mm^2 (0.29 mW total power) at each implanted fiber tip. For stimulations of D1 expressing neurons (Figure 7), a light spot of ~600 μW at the objective was used, resulting in an estimated power density of 141 mW/mm^2 (0.23 mW total power) at the fiber tip. We estimated relative excitation light intensity and excitation area as a function of distance from the fiber tip (Figure 6C) by applying a light scattering model developed by Yona et al.[42] with a scattering coefficient of 140 cm^{-1} approximated for the striatum based on Azimipour et al.[70] and Al-Juboori et al.[71] and an activation threshold for ChR2 of 1 mW/mm^2.[72,73]

Light pulse trains for stimulation (30Hz, 4ms pulse width, 1s or 5/10s durations for DA and D1 neuron stimulation respectively) were programmed in PolyScan2 and triggered with 5V digital pulses controlled via MATLAB and sent from a NIDAQ board (National Instruments PCIe 6343) to the Polygon. Stimulations were triggered randomly (inter-stimulation interval 30-60 seconds) for 5-10 minutes per session for all stimulation experiments.

For the online protocol, see protocols.io: https://doi.org/10.17504/protocols.io.bp2l6xyrklqe/v1.

Freely moving imaging

For visualizing fibers in behaving mice (Figure 3), custom-built miniscopes[34,35] were positioned above the fiber bundle, focused with an XYZ manipulator, and cemented in place with Metabond (Parkell) under brief isoflurane anesthesia. Permanent implantation was used for initial experiments in this study, but baseplate attachment is equally viable. Mice were allowed to recover for 24-48 hrs after

attachment, after which imaging was performed in a custom built acrylic arena as mice foraged for Froot Loops (Kellogg's). The mini-scope GRIN objective had an N.A. of 0.45 for high-efficiency light collection and the imaging area was approximately 800 x 600 μm, allowing visualization of a substantial fraction of the fiber bundle. Packing of fibers into the bundle can be optimized to minimize spacing and imaging field diameter. Both behavioral video and fiber signals were acquired at 30Hz using custom MATLAB acquisition software. Neural imaging data were acquired from DAQ and CMOS PCBs from the UCLA Miniscope project.[62] Illumination intensity was delivered by a 470 nm LED (Luxeon Rebel, Lumileds) at an intensity of 0.1-0.25 mW/mm^2, controlled by a D-A interface (National Instruments USB-6009) and BuckPuck LED controller (LEDdynamics, Inc). Imaging data were motion-corrected with NormCorre,[74] corrected for minor background light leak using spatial high-pass filtering, and converted to $\Delta F/F$. Intensity timeseries for each fiber were extracted using manually selected circular ROIs. Locomotor activity was quantified using manual tracking in ImageJ.

For the online protocol, see protocols.io: https://doi.org/10.17504/protocols.io.bp2l6xyrklqe/v1.

Head-fixed behavior

After grid-implant surgery, the mice recovered for at least one week before handling and behavioral habituation. For reward exper-iments, mice began water scheduling at this time, during which they received 0.8-1.5mL water daily, calibrated so they could main-tain a body weight 85-90% of their free-water body weight, as described previously.[20] Mice were headfixed over a hollow styrofoam ball treadmill (Figure 1B, Smoothfoam, 8in diameter), supported by air in a 3D-printed plastic cradle, which allowed them to run in all directions.[27] To monitor the movement of the ball, two optical mouse sensors (Logitech G203 mice with hard plastic shells removed) were mounted on posts, one at the back and one 90 degrees off to one side of the ball, with the sensors level with the ball's "equator". Pitch and yaw (y- and x-displacement, respectively) were read from the optical mouse sensor at the back, and roll (y-displacement) was read from the optical mouse sensor at the side. The optical mouse sensitivity was set to 400 dpi, polling rate 1kHz. Each optical mouse was connected to a Raspberry Pi (3B+), running a continuous multi-threaded Python program to read in the continuous 1kHz change in x- and y-position (in dots), and output a proportional continuous voltage at 100Hz. The pixels-to-voltage conversion was set such that velocity magnitude of 3.5 m/s[75] corresponded to the maximum output voltage of 3.3V. This velocity magnitude voltage was converted to an analog voltage via a digital-to-analog converter (DAC, MCP4725), and read in through an analog input pin on the NIDAQ board. The sign (direction) of the velocity was sent as a digital binary variable through a separate Raspberry Pi output pin and read in through a separate input pin on the NIDAQ board.

For unpredicted water reward delivery, a water spout mounted on a post delivered water rewards (9 μL, Figure 1B) at random time intervals (randomly drawn from a 5-30s uniform distribution) through a water spout and solenoid valve gated electronically. Licking was monitored by a capacitive touch circuit connected to the spout. Sound stimuli were presented via a USB speaker placed on the table approximately 20 cm in front of the ball (Figure 1B), and calibrated to deliver tones at varying intensities from 80-90 dB, as measured from the location of the mouse. The noise generated by the air supply under the ball treadmill was measured to be approx-imately 78-80 dB. Light stimuli were presented via a LED (Figure 1B, Thor labs, M470L3) mounted on a post level with the mouse, approximately 20 cm away from the ball, 45 degrees contralateral to the implanted side calibrated to deliver light at varying intensities from 1-27mW, as measured just in front of the LED. Salient stimuli were presented in randomized order and at varying intensities, 14-21 presentations of each modality, with intertrial interval randomly drawn from a uniform distribution of 4-40 seconds.

Data was input (licking, velocity, TTLs, etc) and output (to trigger stimulus delivery, reward delivery, LED, image acquisition, etc) at 2kHz by a custom MATLAB program via the NIDAQ card. For synchronization of behavioral data with imaging data, TTLs were sent from the cameras to the NIDAQ card 500μs after the beginning of readout for each frame (Hamamatsu HCLive VSYNC). Behavioral data was then downsampled to match the sampling rate of the neural data by block averaging, i.e., behavioral data was averaged for each frame (binary variables were downsampled in 2 additional ways: rounding and sum).

To record the movements of the jaw (Figure 7B), video recordings were taken using a mounted USB3 camera (Flir Blackfly S USB3 BFS-U3-16S2M-CS), positioned to focus on a side view of the mouse's face. The behavior cameras were triggered on the TTL output from the imaging cameras, as described above.

For the online protocol, see protocols.io: https://doi.org/10.17504/protocols.io.bp2l6xyrklqe/v1.

QUANTIFICATION AND STATISTICAL ANALYSIS

Data were processed and analyzed using built-in and custom lab-written functions in MATLAB (Mathworks, Version 2020b).

Velocity and acceleration

Velocity signals from the optical mice were converted back to m/s for the pitch (forward/backward) and roll (sideways) directions, and to degrees/s for the yaw (rotational) velocity. Pitch and roll combined into a linear velocity measure $= \sqrt{pitch^2 + roll^2}$. To get a measure of overall vigor, we used an "overall velocity" measure, for which we took the sum of the linear velocity and absolute value of the angular velocity (converted to m/s based on the ball circumference), low-pass filtered at 1.5Hz, and then smoothed with a 300ms smoothing window. Overall acceleration was calculated as the moment-to-moment difference of this velocity measure, low-pass filtered at 1.5Hz, and then smoothed with a 300ms smoothing window.

Multifiber photometry preprocessing

Time series movies were motion-corrected using a whole-frame cross-correlation algorithm described previously.[20] Movies were then visually inspected to confirm image stability, and excluded from analysis in cases with excessive motion artifact. Mean fluorescence was extracted from circular regions of interest (ROIs) drawn for each fiber. ROI radius was approximately half that of the fibers (~25-micron diameter ROIs for 50-micron fibers, and ~19-micron for 37-micron fibers). The same ROI map, adjusted to fit each movie, was used for the entire experiment, to ensure consistent ROI identification and mapping over multiple recordings. To calculate the relative change in fluorescence ΔF/F, the mean extracted fluorescence traces were normalized to a baseline (8th percentile fluorescence over a 30s sliding window), to remove any slow frequency changes due to baseline drifts. For the analysis of the two mice with the quasi-simultaneous 470/415nm recordings, in which the 470nm signal was corrected via the 415nm signal (Figures S5I–S5K), the ΔF/F was calculated by first fitting the 415nm signal to the 470nm signal via least squares regression. The fitted signal was calculated as follows:

$$signal_{470}(t) = \beta_0 + \beta_1\, signal_{415}(t) + \varepsilon \qquad \text{(Equation 1)}$$

$$signal_{fitted}(t) = \widehat{\beta}_0 + \widehat{\beta}_1\, signal_{415}(t) \qquad \text{(Equation 2)}$$

The ΔF/F for each timepoint (t) for this analysis was then calculated from the 470nm signal and the fitted signal:

$$signal_{\Delta F/F}(t) = \frac{signal_{470} - signal_{fitted}}{signal_{fitted}} \qquad \text{(Equation 3)}$$

DA release to salient stimuli

To assess the relationship of fluorescence signals to the 1-second salient stimulus presentations while accounting for locomotion changes, peri-event (-1s to 2s around stimulus onset) fluorescence was modeled using a general linear model with overall velocity and acceleration predictors, and stimulus presentation event predictors convolved with a 13 degrees-of-freedom regression spline basis set with 1s duration, generated using MATLAB's *spcol* function. Velocity and acceleration predictors consisted of continuous overall velocity or acceleration at a lag estimated from cross-correlation analyses (+/-500ms lag) of fluorescence vs velocity, and fluorescence vs acceleration, during ITI periods. Velocity and acceleration were then entered as continuous predictors at the lag(s) corresponding to the most positive correlation coefficient (if significant, p<0.05) and the most negative correlation coefficient (if significant, p<0.05). For each fiber, then, there were 0-4 locomotion continuous predictors (0-2 for velocity, and 0-2 for acceleration), and 26 spline predictors (13 for each stimulus modality). We therefore used MATLAB's *fitglm* to fit the following model to each fiber:

$$F = \beta_0 + \sum_{k=1}^{2} \sum_{j=1}^{13} \beta_{jk} x_{jk} + \sum_{l=1}^{2} \sum_{c=1}^{2} \beta_{lc} s_{lc} x_{lc} + \varepsilon$$

Here, F is the ΔF/F fluorescence signal from a single fiber, k = the stimulus modality (light or tone), j = the spline basis function, and x_{jk} is therefore the jth spline basis function convolved with a binary trace that is equal 1 at the times that the onset of stimulus k occurs, and 0 elsewhere. In terms of the locomotion continuous variables, l is the locomotion measure (velocity or acceleration), and c is the relevant cross correlation lags (the lag with the lowest negative correlation coefficient and the lag with the highest positive correlation coefficient); s_{lc} is a binary variable indicating whether the correlation is significant (p<0.05) at that lag, and x_{lc} is the corresponding locomotion continuous variable (velocity or acceleration) at the specified lag.

The resulting salient stimulus event spline predictors and coefficients were then reconstructed into an estimated event-triggered average. Significance of the event-related signal change was determined by whether this estimated event-triggered average exceeded the 99% confidence interval of a bootstrapped null distribution (10000 iterations) for 3 consecutive timepoints (p<1.0x10⁻⁶). To generate the bootstrapped null distribution, we fit the same model using randomly chosen salient stimulus onsets (same number of trials as actual events) instead of the actual event onsets, and reconstructed the estimated event-triggered average, repeated for 10000 iterations.

In Figures S4E–S4H, stimulus presentation trials were separated into trials followed by an acceleration and trials followed by a deceleration, determined by whether the maximum acceleration magnitude during the 1-s stimulus presentation was positive or negative, respectively.

The latency response was determined as the time elapsed between the beginning of the stimulus presentation and when the signal surpassed the half max amplitude (half of the peak or dip amplitude, as applicable) either for the triggered average (Figures 5A and 5B) or on a trial-by-trial basis (Figures 5C–5F). Trial-by-trial signals were reconstructed by regressing out the locomotion, as estimated by the GLM above. Trial-by-trial signals were considered significant if they met 2 criteria: first, the estimated event-triggered average was significant (Figure 4 and as described above), and second, the single-trial response also exceeded the 99% confidence interval of a bootstrapped null distribution (the same null distribution used for the mean) for 3 consecutive timepoints. If the signal crossed back and forth across the half max amplitude threshold multiple times before its peak, the crossing closest to the peak (i.e., the last

crossing before the peak) was considered. The trial-by-trial relative latencies were calculated by subtracting the latency of the first fiber, such that the fiber with the fastest latency had a relative latency of 0.

DA release to optogenetic stimulation

To determine the dopamine response to 1s laser pulses delivered to individual fibers (Figure 6E), we first computed an event-triggered average of the ΔF/F trace for each recording location from 0-0.5 s from the offset of the laser. A significant response was determined by whether this event-triggered average exceeded the 99% confidence interval of a bootstrapped null distribution (10000 iterations) for 3 consecutive timepoints ($p < 1.0 \times 10^{-6}$). The bootstrapped null distribution was determined by computing an event-triggered average from n randomly selected timepoints, excluding the 1s laser pulses, where n is the number of stimulation trials, repeated for 10000 iterations. The triggered average plots (Figure 6F, bottom) show the event triggered average from 0-2 s from the offset of the laser, smoothed using a moving average window of 0.3 seconds.

In order to determine the relationship between the stimulated response and distance from the stimulated location in each dimension (Figure 6G), we first computed the average ΔF/F for each recorded location and trial (inclusion criteria described below) within 0-0.5 seconds after the offset of the 1s laser pulses. We then averaged these responses across trials for each stimulated fiber. The distance vector from the tip of the stimulated fiber to the tip of the recorded fiber in each dimension was computed by subtracting the position (determined from the CT scan as described above) of the stimulated fiber from the position of the recorded fiber. We then pooled all the responses for each stimulation (inclusion criteria described below), and binned them by distance into 12 evenly distributed bins for each dimension (bin widths, M/L: 0.33 mm, A/P: 0.49, D/V: 0.38), and averaged the responses within each bin. Error bars, SEM.

To determine the relationship between the stimulated response and the distance between the recording location and stimulation location (Figure 6H), we fit an exponential regression model using MATLAB's *fit* function of the form:

$$y = a * e^{bd}$$

Where *y* is the stimulated response, calculated as described above, and *d* is the euclidean distance between the position of the recording location and the stimulation location (i.e., the length of the distance vector), calculated using MATLAB's *norm* function:

$$d = \sqrt{(x1_{ML} - x2_{ML})^2 + (x1_{AP} - x2_{AP})^2 + (x1_{DV} - x2_{DV})^2},$$

where *x*1 is the position of the recorded fiber and *x*2 is the position of the stimulated fiber. The shaded region show the 95% confidence interval of the predicted curve.

Inclusion criteria for the above analyses were three-fold. First, to be included in any of the analyses, the position of the fiber tip had to be within, or on the border of, the striatum, determined as described above (24 recording locations). Second, to confirm expression of the opsin, we only included stimulated locations for which 1s laser pulses evoked a significant rDAm3.0 response in at least one other location (18 out of 24 included locations). This was because a significant response at the stimulation site could be due to photoswitching of the rDAm3.0 (see Figures 6E and S7A). Third, to confirm expression of the sensor, we only included recording locations for which a significant response (defined above) was observed for at least one set of stimulations (22 out of 24 included locations).

For control mice expressing tdTomato instead of rDAm3.0, all recording locations within or on the border of the striatum were included. For control mice expressing rDAm3.0 but no opsin, we included recording locations within or on the border of the striatum and had expression confirmed by a significant reward response (mean exceeding 99% confidence interval of the bootstrapped null distribution for 3 consecutive timepoints, $p < 1.0 \times 10^{-6}$).

Behavior response to optogenetic stimulation

In order to measure movements of the jaw in response to optogenetic stimulation of D1 neurons, a Python based toolbox called DeepLabCut[47,48] was used. The side-view recordings of the mouse's face (Figure 7B) were uploaded onto Google Drive to be processed using DeepLabCut via Google Colab. Six points (spout, nose, upper jaw, front lower jaw, middle lower jaw, and back lower jaw) were manually labeled in 20 random frames each (selected using k-means algorithm) from 10 training videos across 3 different mice. The model was trained using the pretrained ResNet50 network for 300,000 iterations or until the loss plateaued. Low certainty labels were then manually corrected and merged with the previous training set to be trained again for another ∼300,000 iterations. This correction process was repeated 3 more times to account for changes in the lighting and zoom of the behavior videos. The final version was trained on 24 different videos across 5 different mice. The rest of our videos were labeled automatically using this final trained model. To quantify the jaw movement, we used the position of the front lower jaw as it appeared to be the most isolated marker for the jaw. The jaw velocity was calculated as the total displacement (in pixels) per frame:

$$v_{jaw} = \sqrt{(x_t - x_{t-1})^2 + (y_t - y_{t-1})^2} * F,$$

where x and y are the coordinates of the front lower jaw marker at time t. We only included timepoints in which the likelihood of the DeepLabCut label was greater than 0.99 for at least 10 frames in a row. In frames with a likelihood of less than 0.99 the jaw

was typically obscured by the mouse's paw or tongue. The change in jaw movement due to stimulation was assessed via a jaw velocity change index:

$$(v_{stim} - v_{baseline}) / (v_{stim} + v_{baseline}),$$

where v_{stim} is the average jaw velocity during the first 5 seconds of stimulation, and $v_{baseline}$ is the average jaw velocity during the 5s before stimulation. The change in jaw velocity was averaged across trials for a given stimulation pattern. Significance was determined by whether this average exceeded the 99% confidence interval of a bootstrap distribution. The bootstrap distribution was estimated by randomly selecting new timepoints to calculate the above average using 10,000 iterations. To determine the effect of mouse group and stimulation location, we performed a two-way ANOVA on the change in jaw velocity. To subsequently determine the effect of mouse group (opto vs control, Figure 7D), we performed a two sample t-test on the change in jaw velocity.